Pergamon

Geochimica et Cosmochimica Acta, Vol. 68, No. 11, pp. 2591–2611, 2004

0016-7037/04 $30.00 + .00

doi:10.1016/j.gca.2003.10.033

Oxygen isotopic evolution of amoeboid olivine aggregates in the reduced CV3 chondrites Efremovka, Vigarano, and Leoville

T. J. FAGAN,[1,*] A. N. KROT,[2] K. KEIL,[2] and H. YURIMOTO[1]

[1]Department of Earth and Planetary Sciences, Tokyo Institute of Technology, 2-12-1 Ookayama, Meguro, Tokyo 152-8551, Japan
[2]Hawai'i Institute of Geophysics and Planetology, School of Ocean and Earth Science and Technology, University of Hawai'i at Manoa, Honolulu, HI 96822, USA

(*Received March* 27, 2003; *accepted in revised form October* 29, 2003)

Abstract—Amoeboid olivine aggregates (AOAs) from the reduced CV chondrites Efremovka, Vigarano, and Leoville consist of forsteritic olivine, FeNi-metal and a refractory component composed of spinel, Al-diopside, ±anorthite. Secondary ferrous olivine and alkali-rich minerals (nepheline and sodalite), commonly observed in the oxidized CVs, are rare. Mineralogy and chemical compositions of AOAs are similar to those predicted by equilibrium thermodynamic condensation models, suggesting that AOAs formed primarily by gas-solid condensation over a narrow temperature range, slightly below the temperatures over which most Ca-Al-rich inclusions (CAIs) formed. AOAs in the reduced CVs preserve a 1st-generation ^{16}O-rich signal ($\delta^{17,18}O \sim -40‰$) similar to that observed in many CAIs, suggesting that these refractory objects originated from a common source in the solar nebula. In fact AOAs and many fine-grained CAIs may have formed by the same processes, but at slightly different temperatures, and can be considered a single class of refractory objects.

Alteration of the AOAs is manifested by differing extents of ^{16}O-depletion in original AOA minerals, FeO-enrichment in olivine, and formation of interstitial very fine grained Na-bearing phases. From the six AOAs and one fine-grained, melilite-pyroxene-rich CAI examined in this study, five distinct patterns of alteration were identified. (1) One unaltered AOA from Vigarano is characterized by ^{16}O-rich forsterite without FeO-rich rims and interstitial Na-bearing phases. (2) Weak alteration in the melilite-pyroxene-rich CAI is characterized by incomplete ^{16}O-depletion in some melilite and precipitation of Na-bearing phases near the CAI rim. (3) Oxygen isotopic composition and mineralogy are correlated in two AOAs from Leoville with ^{16}O-rich olivine, ^{16}O-poor anorthite and a range of intermediate compositions in Al-diopside. This pattern is consistent with model diffusion between original grains and a ^{16}O-poor reservoir during a relatively short-term (<60 yr), high-temperature (900–1100°C) event. (4) Original forsterite has been enriched in FeO, but remained ^{16}O-rich in one AOA from Vigarano. This result is consistent with the slower rate of diffusion of O than Fe and Mg in olivine. At least some interstitial phases are ^{16}O-rich, and Na-bearing phases are abundant in this AOA. (5) In contrast, oxygen isotopic composition and Fo-content are correlated in two AOAs from Efremovka. The olivine in these AOAs tends to have forsteritic ^{16}O-rich cores and FeO-rich ^{16}O-depleted rims. The general correlation between oxygen isotopic composition and Fo-content is difficult to model by diffusion, and may have formed instead by aqueous dissolution and precipitation along the margins of preexisting olivine grains.

Independent evidence for aqueous alteration of the Efremovka AOAs is provided by OH-rich signals detected during ion beam sputtering of some of the ^{16}O-poor olivine. Elevated ^{16}OH-count rates and order of magnitude increases in ^{16}OH detected during single analyses reflect trapping of an aqueous phase in ^{16}O-depleted olivine. An elevated ^{16}OH signal was also detected in one analysis of relatively ^{16}O-poor melilite in the melilite-pyroxene CAI from Vigarano, suggesting that this object also was altered by aqueous fluid. *Copyright © 2004 Elsevier Ltd*

1. INTRODUCTION

Oxygen isotopic compositions of Ca-Al-rich inclusions (CAIs) from chondritic meteorites show that most of them formed in an unusual ^{16}O-rich setting (Clayton et al., 1973, 1977; Yurimoto et al., 1994, 1998; McKeegan et al., 1998; Guan et al., 2000; Fagan et al., 2001; Aléon et al., 2002). The oxygen isotopic compositions combined with petrologic studies indicate that, as the components of chondrites were beginning to form, a portion of the solar nebula hot enough to prevent forsterite condensation was anomalously enriched in ^{16}O (for early studies based on Allende, see Grossman, 1972, 1975; see MacPherson et al., 1988, for a review; also, Yurimoto et al., 1994; Russell et al., 1998; Fagan et al., 2000; Guan et al., 2000; Krot et al., 2001a). Subsequent stages of CAI processing, possibly involving remelting (Yurimoto et al., 1998; Aléon et al., 2002; Makide et al., 2002) and parent-body alteration (Young and Russell, 1998; Wasson et al., 2001; Fagan et al., 2002), resulted in isotopic shifts due to mass-dependent fractionation and isotopic exchange with ^{16}O-poor reservoirs.

Amoeboid olivine aggregates (AOAs) formed in a nebular setting below forsterite condensation temperatures and thus record petrogenesis over a temperature interval not sampled in detail by CAIs (Grossman and Steele, 1976; Kornacki and Wood, 1984; Hashimoto and Grossman, 1987; Komatsu et al.,

* Author to whom correspondence should be addressed, at Department of Mineral Science, National Museum of Natural History, Smithsonian Institution, Washington, DC 20013-7012, USA (fagan.tim@nmnh.si.edu).

2001; Krot et al., 2002a). Abundances of Na-, Cl-, and FeO-bearing minerals vary widely among AOAs from different chondrite groups. The origin of these relatively volatile phases has been attributed variously to low-temperature condensation in a nebular setting (Grossman and Steele, 1976; Hashimoto and Grossman, 1987) and parent body alteration in the presence of an aqueous fluid (Michel-Lévy, 1986, Komatsu et al., 2001; Chizmadia et al., 2002; Imai and Yurimoto, 2003). Oxygen isotopic results indicate that early stages of AOA-formation took place in a ^{16}O-rich setting, similar to the setting in which CAIs formed, whereas alteration took place in a ^{16}O-poor setting (Hiyagon and Hashimoto, 1999; Aléon et al., 2002; Krot et al., 2002a; Imai and Yurimoto, 2003).

Considered alone, these results could be interpreted as a consequence of a simple transfer of refractory objects from a ^{16}O-rich nebular setting to a ^{16}O-poor parent body; however, this contradicts evidence in coarse-grained CAIs (CGIs) from the CV chondrites for the existence of both ^{16}O-rich and ^{16}O-poor gases in the nebula. Most notably, CGIs from the CV chondrites exhibit a characteristic pattern in oxygen isotopic compositions: most melilite and anorthite are ^{16}O-poor, some melilite and anorthite are variably exchanged, fassaite shows no or minor depletion in ^{16}O, and spinel has fully retained its original ^{16}O-rich isotopic composition (Clayton et al., 1977; Clayton, 1993; Yurimoto et al., 1994, 1998; Kim et al., 2002). Comparison of oxygen isotopic systematics in fine- and coarse-grained CAIs from the CV Efremovka indicates that Efremovka CGIs attained their characteristic oxygen isotopic compositions before formation of the parent body, most likely in the nebula (Fagan et al., 2002). The same is probably also true of CGIs from the other CV chondrites. The presence of ^{16}O-poor melilite in CV CGIs, combined with uniformly ^{16}O-depleted CAIs in CH, CB and enstatite chondrites (Sahijpal et al., 1999; Krot et al., 2001a; Fagan et al., 2001), indicate that either multiple CAI-forming regions with distinct oxygen isotopic compositions existed simultaneously, or the oxygen isotopic composition of CAI-forming regions varied through time.

In this context, AOAs from the CV chondrites provide an important constraint on oxygen isotopic evolution in the solar nebula. If the CV AOAs are ^{16}O-poor, then the CGI melilite might have exchanged oxygen with a reservoir that remained ^{16}O-poor as temperature dropped. If the CV AOAs are ^{16}O-rich, then fluctuations in isotopic composition, temperature, or both are required to account for the oxygen isotopic systematics in refractory objects from CV chondrites. Analyses of AOAs in the CVs Yamato-86009 (Hiyagon and Hashimoto, 1999), Efremovka (Krot et al., 2002a), and Allende (Imai and Yurimoto, 2003) suggest the latter; however, only one CV AOA was analyzed in each of these studies. Furthermore, it has not been established whether CV AOAs underwent isotopic alteration with nebular gases. If so, it may be possible that refractory objects from the CVs are anomalous, as CAI minerals from many other groups yield homogeneous oxygen isotopic compositions that do not require interactions with gases of variable isotopic composition (McKeegan et al., 1998; Sahijpal et al., 1999; Fagan et al., 2001; Guan et al., 2000; Krot et al., 2002a).

In this study we review the mineralogy and determine in situ oxygen isotopic compositions in AOAs from the reduced CV chondrites Efremovka, Leoville, and Vigarano. This study builds on the petrogenetic framework established by Komatsu et al. (2001). Our main goals are to: (1) confirm whether AOAs originated in a ^{16}O-rich setting, similar to most CAIs; and (2) determine if systematic variations in mineralogy, textures, and oxygen isotopic compositions can be used to assess the setting and physical conditions under which AOAs were altered. To evaluate time-scales and mechanisms of alteration, we model O-diffusion in a variety of AOA minerals and Fe-Mg-diffusion in olivine, and compare model results with observed textures and compositions.

2. ANALYTICAL METHODS

2.1. Petrography and Mineral Compositions

Amoeboid olivine aggregates were identified in three polished thin sections of Efremovka (E36), Vigarano (USNM 6295-5) and Leoville (UH 122-1) previously studied by Komatsu et al. (2001). An optical image of each thin section was obtained using apparatus designed for scanning of 35 mm photographic slides. All AOAs, CAIs, and chondrules greater than $\sim$ 100 μm across were mapped. Mapping of AOAs was guided by large-scale X-ray elemental maps (typically, Mg, Al, Ca, Si and Ti Kα) collected using a Cameca SX-50 electron microprobe at the University of Hawai'i (UH). Minerals and textures were examined using petrographic microscopes, and secondary and back-scattered electron imaging (SEI and BSE, respectively); the electron images were collected using the UH Cameca SX-50 and a JEOL JSM-5310LV scanning electron microscope with an Oxford LINK-ISIS EDS detector at Tokyo Institute of Technology (Titech). The EDS detector was used to collect quantitative mineral analyses with a $\sim$ 1 μm beam and 1 nA current. Selected minerals were analyzed by wavelength dispersive spectroscopy (WDS) using a JEOL JXA-8800 electron microprobe at Titech. The WDS analyses were based on well-characterized oxide and silicate standards and were collected using: 15 keV accelerating voltage; 1 μm spot-size; 12 nA current; peak and background counting times of 12 to 30 s; and a JEOL-supplied ZAF program to account for matrix effects.

2.2. Ion Microprobe Analyses

In situ oxygen isotope analyses were collected using a modified Cameca 1270 ion microprobe at Titech. A primary ion beam of mass filtered positive Cs ions accelerated to 20 keV was used to excavate shallow pits ranging from 3 to 10 μm across. The primary current was adjusted for each measurement to obtain a count rate of negative ^{16}O ions of $\sim$3.5 to 4 $\times$ 10^5 cps. A normal-incident electron gun was used for charge compensation of analyzed areas. Negative secondary ions from the ^{16}O tail, ^{16}O, ^{17}O, ^{16}OH, and ^{18}O were analyzed at a mass resolution power of $\sim$6000, sufficient to completely separate hydride interference on ^{17}O. Secondary ions were detected by an electron multiplier in pulse counting mode, and analyses were corrected for dead time. Matrix effects under these operating conditions at Titech have been examined by comparing analytical results for a variety of minerals with known oxygen isotopic composition, including SPU spinel (from Russia), anorthite (Miyake-jima, Japan), augite (Takashima, Japan), and synthetic gehlenite and åkermanite. The reproducibility of $^{17 \text{ or } 18}$O/^{16}O on different analysis points from the same standard was $\sim$ $\pm$ 5‰ ($\pm 1\sigma$). Matrix effects on detected oxygen isotopic composition among the minerals analyzed are also limited to $\sim$ 5‰. Therefore, we used one standard, the SPU spinel, to determine instrumental mass fractionation during each analytical session. Overall errors in accuracy are estimated to be $\sim$ $\pm$ 5‰ ($\pm 1\sigma$) for each analysis. In addition to these random errors, we suspect that two analytical sessions (A3 and B10) were affected by systematic errors in instrumental mass fractionation that displaced results to the ^{18}O-rich side of the carbonaceous chondrite anhydrous mineral line (CCAM), as discussed in Results. We note, however, that all of our results are within $\pm$10‰ ($\pm 2\sigma$ in accuracy) of CCAM.

Areas selected for analyses were imaged in BSE or SEI before and after sputtering to verify mineralogy. Most of the sputtered pits are located entirely or nearly so (>90%) in a single mineral. However, due to the fine grain size, several analysis pits overlap on significant

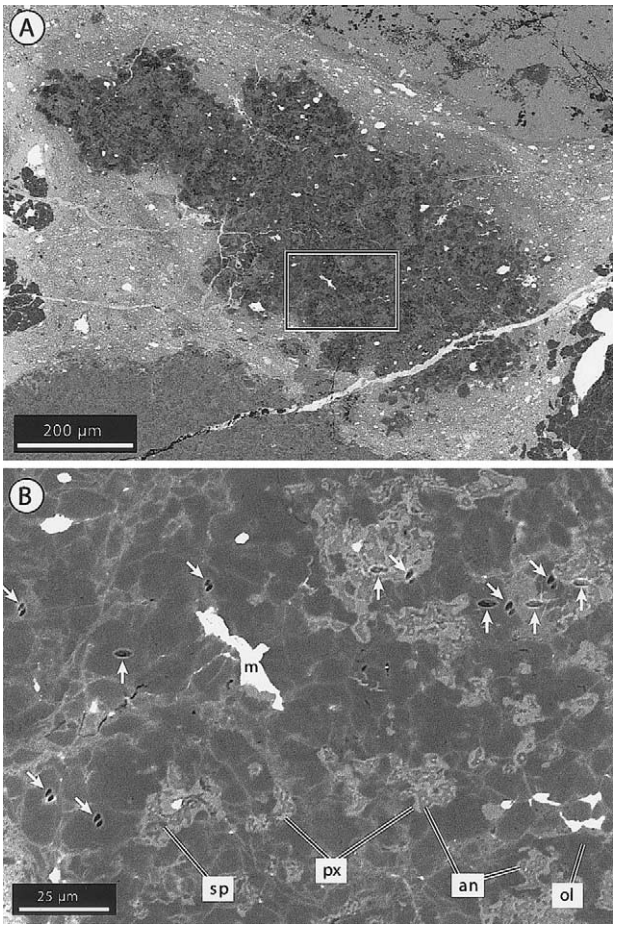

Fig. 1. Backscattered electron images (BSEs) of Efremovka AOA-23. (A) Dark gray grains are olivine; medium gray regions are fine-grained mixtures of Al-diopside, anorthite and minor spinel; white grains are predominantly FeNi-metal, some are troilite. Area enclosed by box shown in detail in (B). (B) Olivine (ol) grain boundaries are relatively FeO-rich. Al-diopside (px) is lighter gray than anorthite (an) and encloses anorthite and spinel (sp). Bright grains are FeNi metal (m). Metal grains are partially oxidized, but the oxidation is not apparent under the grayscale setting of this image. Craters excavated during SIMS analyses from two analytical sessions are highlighted by the arrows, and from left to right are: A2-2, A2-5, A2-6, B5-6, A2-1, B5-1, A2-10, B5-4, A2-9, B5-3, A2-8, and B5-2.

fractions of two or more minerals, or on distinct textural domains of a single mineral (e.g., rims and cores of zoned olivine).

3. RESULTS

3.1. Efremovka AOAs 23 and 55

3.1.1. Textures and mineralogy

In thin section, Efremovka AOA-23 is an elongate object (~1000 × 300 μm) with an irregular surface morphology (Fig. 1A). It is composed dominantly of granular olivine and a refractory component consisting of finely intergrown Al-diopside, anorthite and minor spinel. The refractory component is evenly dispersed throughout the AOA. Grains of FeNi-metal are widespread, but in minor mode. Troilite is rare, but does occur as fine grains included in or interstitial to olivine.

The olivine in AOA-23 consists of closely-packed, equant to slightly elongate, anhedral grains on the order of 2 to 10 μm in diameter, but ranging up to ~ 20 μm across (Fig. 1B). The seams along olivine grain boundaries are enriched in iron, and form iron-rich patches where multiple grain boundaries coalesce (Fig. 1B). One iron-rich grain was identified (Fig. 1B) and yields a stoichiometric mineral formula with Fo_{90} in contrast to compositions near Fo_{99} for the more abundant magnesian olivine (Table 1). Olivine also appears to be slightly enriched in iron in halos around tiny troilite inclusions. The metal grains in contact with olivine appear to be partly oxidized, but generally are not associated with Fe-rich halos in neighboring olivine grains.

The refractory component in AOA-23 is dominated by fine-grained Al-diopside and anorthite with minor spinel (Fig. 1B). As indicated in previous studies of AOAs (Komatsu et al., 2001; Chizmadia et al., 2002; Itoh et al., 2002), the anorthite is partially to completely enclosed by Al-diopside and tends not to be in contact with olivine. Where spinel is present, it tends to be enclosed within anorthite.

Efremovka AOA-55 is larger than AOA-23 (Fig. 2A). It has an elongate triangular shape in thin section and a jagged external boundary. Several small fragments of AOA-55 are not connected in the plane of the thin section to the main body of the AOA, giving the appearance of “islands” off of a jagged “coastline.”

Like AOA-23, AOA-55 consists mostly of forsterite and an Al-diopside-bearing refractory component, with minor FeNi-metal; however, this AOA is composed of two distinct textural domains. The more abundant variety, which occupies the outer portions, is dominated by branching monomineralic bands of forsterite and spinel separated by intervening bands of diopside with variable Al-contents (Fig. 2B). The bands tend to be curved, and the ratio of olivine:refractory component is relatively low. The core of the AOA is characterized by granular olivine with refractory nodules and a higher modal abundance of olivine (Fig. 2C). The texture of the granular olivine domain is generally similar to that of AOA-23. The refractory component in this domain consists mostly of Al-diopside, which commonly encloses spinel. Spinel in the interiors of the refractory nodules is characterized by multiple tiny inclusions of Al-diopside. Similar to AOA-23, these olivine grain boundaries are FeO-enriched. This contrasts with the branching domain of AOA-55, where no FeO-enrichment is observed along grain boundaries (Fig. 2B). Very fine (<1μm) FeO-rich grains, possibly of hercynite, are associated with Mg-spinel in rare cases in the branching domain.

3.1.2. Oxygen isotopic analyses

Forsterite from Efremovka AOA-23 is dominated by ^{16}O-rich values near −40‰ $\delta^{17,18}O$, but with a range extending from ~ −30 to −50‰ $\delta^{17,18}O$ (Table 2, Fig. 3). Iron-rich olivine, an Al-diopside+spinel mixture, and mixtures of anorthite and Al-diopside form a ^{16}O-depletion trend from the ^{16}O-poor end of the forsterite range to ~ −20‰ $\delta^{17,18}O$. No correlation between oxygen isotopic composition and anorthite: Al-diopside ratio was observed in the mixed analyses.

Table 1. Representative electron microprobe analyses (wt %) of olivine and melilite.[a]

	Efremovka AOA-23			Vigarano AOA-65		Vigarano AOA-66			Vigarano CAI-67		
Mineral	Mg-rich olivine	Mg-rich olivine	Fe-rich olivine	Mg-rich olivine	Mg-rich olivine	Mg-rich olivine	Mg-rich olivine	Fe-rich olivine	Melilite	Melilite	Melilite
SiO_2	42.5	42.7	39.4	42.1	42.4	41.4	42.0	36.7	23.3	24.8	24.3
Al_2O_3	<0.05	<0.05	0.66	<0.05	<0.05	<0.05	<0.05	0.29	34.1	32.2	32.8
Cr_2O_3	<0.12	<0.12	0.22	0.19	0.18	<0.12	<0.12	<0.12	<0.12	<0.12	<0.12
FeO	1.67	0.94	9.61	0.31	0.10	4.22	2.96	26.8	0.25	0.49	0.11
MnO	0.11	<0.04	0.21	<0.04	0.06	0.12	0.05	0.19	<0.04	<0.04	0.05
MgO	55.1	55.2	47.8	56.7	56.2	53.3	53.9	34.1	5.28	2.81	1.56
CaO	0.18	0.23	0.13	0.18	0.15	0.07	0.09	0.14	35.8	37.5	39.7
Na_2O	<0.05	<0.05	<0.05	<0.05	<0.05	<0.05	<0.05	<0.05	0.09	0.13	<0.05
K_2O	<0.03	<0.03	<0.03	<0.03	<0.03	<0.03	<0.03	<0.03	<0.03	<0.03	0.04
total	99.6	99.1	98.1	99.6	99.1	99.1	99.0	98.2	98.93	98.09	98.68
	Structural formulae based on 4 O (olivine) and 7 O (melilite)										
Si	1.01	1.01	0.99	0.99	1.00	1.00	1.01	1.00	1.06	1.15	1.12
Al	b.d.	b.d.	0.019	b.d.	b.d.	b.d.	b.d.	0.009	1.83	1.75	1.78
Cr	b.d.	b.d.	0.004	0.003	0.003	b.d.	b.d.	b.d.	b.d.	b.d.	b.d.
Fe	0.033	0.019	0.201	0.006	0.002	0.085	0.059	0.61	0.009	0.019	0.004
Mn	0.002	b.d.	0.005	b.d.	0.001	0.002	0.001	0.004	b.d.	b.d.	0.002
Mg	1.95	1.95	1.78	1.99	1.98	1.91	1.93	1.38	0.359	0.194	0.107
Ca	0.005	0.006	0.003	0.005	0.004	0.002	0.002	0.004	1.75	1.86	1.96
Na	b.d.	b.d.	b.d.	b.d.	b.d.	b.d.	b.d.	b.d.	0.008	0.012	b.d.
K	b.d.	b.d.	b.d.	b.d.	b.d.	b.d.	b.d.	b.d.	b.d.	b.d.	0.002
total	2.99	2.99	3.00	3.00	2.99	3.00	2.99	3.00	5.03	4.98	4.99
Fo, Åk	98	99	90	100	100	96	97	69	36	19	11

[a] b.d. = below detection.

Elevated OH was detected during one analysis (A2-2) and a replicate (A2-3) collected immediately afterward on the same spot of a FeO-rich olivine grain margin (Table 2; Fig. 1B). During analysis A2-2, ^{16}OH-intensities jumped by nearly an order of magnitude (Fig. 4A). The OH-signal in these analyses remained high after the jump, in contrast to occasional spikes in ^{16}OH-signal observed during other analyses (Fig. 4B). Cycles collected after the jump in ^{16}OH are more depleted in ^{16}O than cycles before the jump, but both pre- and postjump cycles are ^{16}O-poor relative to results from forsterite. Thus, the ^{16}O-depleted composition of A2-2 is due to all micro-domains sampled during sputtering. In the duplicate analysis (A2-3), only four prejump cycles were collected; these probably reflect slight movement of the stage between analyses or sputtering of powder that fell back into the crater. Isotopic results from these cycles are not distinct from the postjump cycles.

As in AOA-23, most of the forsterite from AOA-55 is enriched in ^{16}O in comparison to FeO-rich olivine grain boundaries (Fig. 3B). Iron-rich grain boundaries were not identified in the branching textural domains of AOA-55; however, an analysis collected along a forsterite-forsterite grain boundary yielded a ^{16}O-depleted composition (analysis B2-1; Table 2; Figs. 2B and 3B). The count rate of ^{16}OH increased by a factor of approximately four during this analysis, indicating sputtering of an OH-rich micro-domain similar to analysis A2-2.

Most analyses of other phases from AOA-55, including Al-diopside, spinel, and mixtures of Al-diopside+olivine and Al-diopside+spinel, fall in the same range as the olivine (Table 2; Figs. 3B, C). The one exception is a ^{16}O-rich spinel (A3-2), which is hardly surprising given the tendency of spinel to retain a ^{16}O-rich composition even in altered CAIs (Clayton et al., 1973; Clayton, 1993; Yurimoto et al., 1994); however, two other spinel analyses are relatively depleted in ^{16}O. Enstatite in a ferro-magnesian chondrule adjacent to AOA-55 is ^{16}O-poor.

Some of the analyses (e.g., B2-2 and B4-4 of AOA-55 forsterite) fall near or slightly in excess of 2σ of analytical precision to the ^{18}O-rich, ^{17}O-poor side of CCAM (Fig. 3). Several of these are from one analytical session (A3) and may have been affected by an erroneous estimate of instrumental mass fractionation. Given the predominance of results within 2σ of CCAM (Fig. 3), we do not consider the ^{18}O-rich/^{17}O-poor data points indicative of a significant fractionation from values near CCAM.

3.2. Leoville AOAs 7 and 8

3.2.1. Textures and mineralogy

Leoville AOAs 7 and 8 have previously been described by Komatsu et al. (2001; their figs. 1B,C, 2, and 3), and our observations confirm their results. Leoville AOA-8 is large and triangle-shaped with an irregular surface (Fig. 5A). It consists of forsterite with a granular texture and refractory domains composed of Al-diopside and anorthite with minor spinel. The refractory domains are distributed evenly throughout much of the AOA, but one area is dominated by the refractory component (Fig. 5B). Al-diopside forms mantles of the refractory domains and shares grain boundaries with neighboring olivine; anorthite is enclosed by and shares convoluted grain boundaries with Al-diopside; spinel occurs as fine grains with indistinct crystal boundaries within anorthite (Fig. 5C). Some of the spinel grains have a mottled texture and appear to be partially altered to FeO-bearing submicron-sized grains.

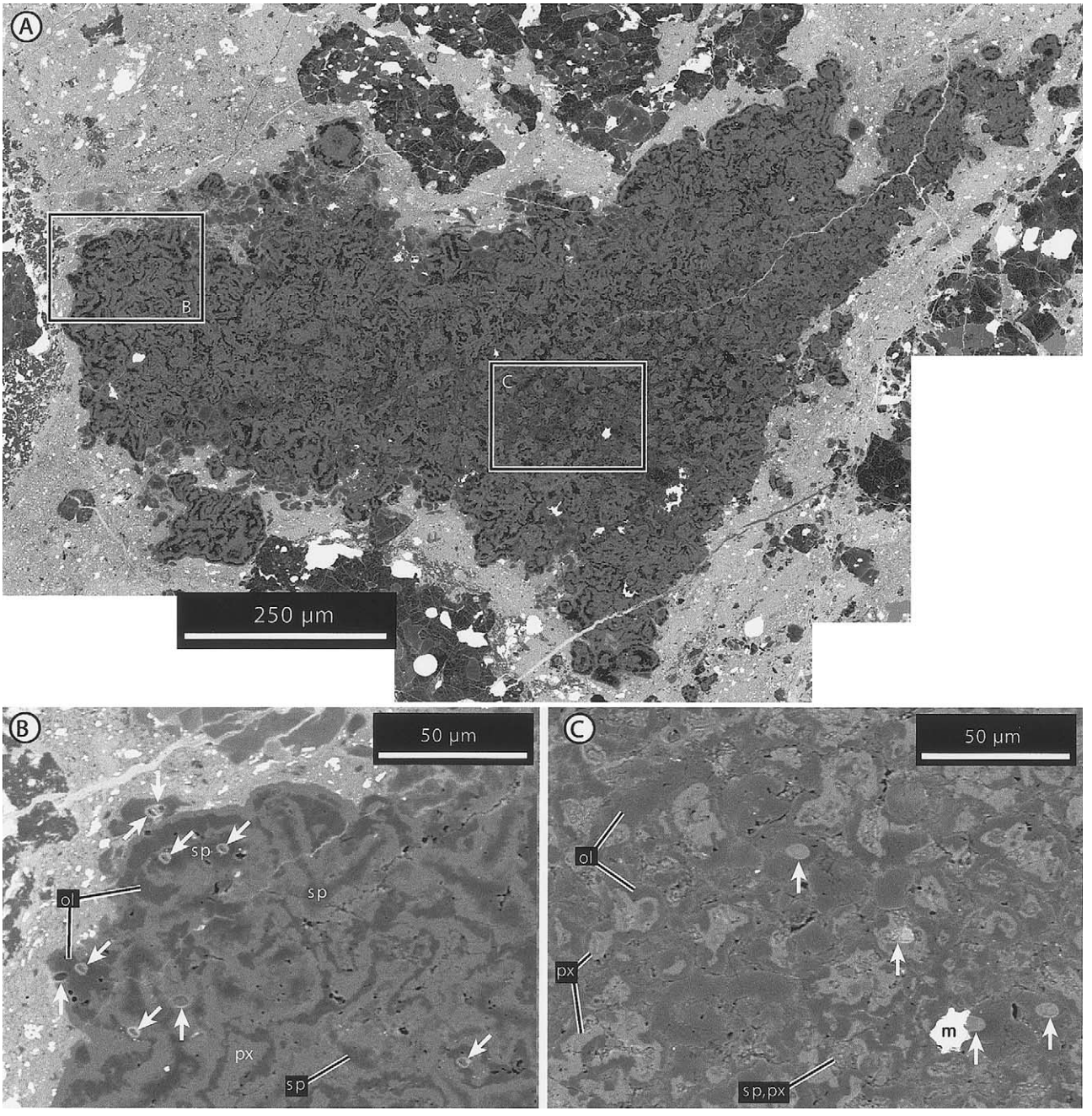

Fig. 2. (A) Mosaic of BSE images of Efremovka AOA-55. Most of the AOA has a branching texture (B), but a region in the core is dominated by granular olivine (C). Panels (B) and (C) both consist of a BSE image with a secondary electron (SEI) overlay. In each composite, a small percentage of the SEI overlay is transmitted, so that the resulting image shows mineral textures dominated by BSE contrast and sputtered craters dominated by SEI contrast. (B) Elongate strands of forsterite and spinel interlayered with diopside with variable Al-content form the branching texture. The upper traverse of craters sputtered during SIMS analyses are, from left to right: B1-2 and B2-2 (same spot); B2-3; and B2-4. The lower set of craters are, from left to right: B1-1; B2-1; B2-5; A3-1; and B2-6. (C) Granular texture is dominated by equant olivine grains. Seams between grains are enriched in FeO. Craters sputtered during SIMS analyses are, from left to right: B3-6; B3-5; B3-3; and B3-4. Al-diopside encloses spinel with tiny islands of Al-diopside (sp,px). Mineral abbreviations as in Figure 1.

Most of AOA-7 consists of granular forsterite with some FeNi-metal and only a minor fraction of refractory component. One region, however, consists of fine-grained Al-diopside and anorthite, and appears to be a CAI enclosed within the AOA (Fig. 5D). Some sodic alteration was identified in this CAI region by Komatsu et al. (2001), but this appears to be of minor extent. The CAI-region is mantled by a semicontinuous band of Al-diopside. Some

Table 2. Oxygen isotopic results (‰ relative to SMOW).[a]

Analysis	Sputtered material (%)	$\delta^{17}O$	$\delta^{18}O$	$1\sigma^{17}O$	$1\sigma^{18}O$
Efremovka AOA-23					
A2-1	fo (100)	−34.7	−33.8	2.1	1.7
A2-2	olv (100, fo with FeO-rich g.b.)[b]	−16.9	−17.9	3.0	2.5
A2-3	olv (100, fo with FeO-rich g.b.)[b]	−21.7	−19.9	3.2	2.1
A2-4	fo (100)	−36.9	−34.7	2.4	1.9
A2-5	olv (100, fo with FeO-rich g.b.)[c]	−28.7	−28.1	2.3	1.8
A2-6	fo (100)	−41.4	−36.0	2.4	1.5
A2-7	fo (100)	−46.8	−43.7	2.5	1.7
A2-8	fo (99), Aldi (tr)	−36.8	−35.5	1.9	1.5
A2-9	fo (95), Fe-olv (5)	−42.8	−41.6	2.2	1.5
A2-10	an (75), Aldi (15), fo (10)	−20.5	−21.4	2.3	1.4
B5-1	an (50), Aldi (50)	−22.2	−19.2	2.3	1.6
B5-2	an (50), Aldi (50)	−27.3	−23.6	2.5	1.7
B5-3	Fe-olv (95), fo (5)	−30.3	−28.7	2.2	1.5
B5-4	fo (100)	−46.5	−35.8	2.0	1.6
B5-5	fo (100)	−43.2	−36.0	2.8	1.6
B5-6	fo (100)	−37.1	−39.1	2.4	1.5
B5-7	an (60), Aldi (40)	−31.8	−36.1	2.3	1.5
B5-8	fo (100)	−36.0	−36.9	2.7	1.7
B5-9	fo (100)	−41.1	−37.6	2.3	1.6
B5-10	Aldi (70), spn (30)	−32.9	−25.5	2.4	1.5
Efremovka AOA-55					
A3-1	Aldi (100)	−44.4	−31.8	2.3	1.5
A3-2	spn (100)	−51.0	−42.1	2.2	1.4
A3-3	Aldi (100)	−43.8	−35.3	2.5	1.5
B1-1	fo (90), di (10)	−42.9	−36.3	2.1	1.4
B1-2	fo (100)	−38.3	−38.4	2.4	1.9
B2-1	olv (100, fo with g.b.)[b]	−26.8	−25.9	2.9	2.3
B2-2	fo (100)	−44.3	−31.5	2.1	1.5
B2-3	spn (100)	−36.6	−30.0	2.1	1.7
B2-4	spn (100)	−34.6	−34.6	2.2	1.5
B2-5	di (90), fo (10)	−38.8	−28.2	2.5	1.7
B2-6	fo (100)	−37.9	−30.0	2.8	1.9
B3-1	fo (60), Aldi (40)	−29.0	−29.2	1.9	1.6
B3-2	Aldi (60), fo (40)	−23.5	−27.1	2.5	1.5
B3-3	fo (100)[d]	−39.1	−39.2	2.1	1.4
B3-4	olv (100, fo with FeO-rich g.b.)[b]	−26.1	−32.4	2.4	1.5
B3-5	spn (50), Aldi (50)	−32.2	−31.6	2.4	1.4
B3-6	fo (100)	−40.5	−37.2	2.2	1.3
B3-7	spn (75), Aldi (25)	−41.1	−40.8	2.2	1.6
B3-8	fo (100)	−44.2	−43.7	2.7	1.6
B4-1	Aldi (60), spn (40)	−34.9	−32.1	2.1	1.9
B4-2	olv (50), Aldi (50)	−38.5	−30.9	2.1	1.8
B4-3	olv (100, fo with FeO-rich g.b.)	−34.9	−29.7	2.2	2.0
B4-4	fo (100)	−41.9	−32.2	2.5	1.9
B4-6	olv (100, fo with FeO-rich g.b.)	−30.5	−34.3	2.7	3.3
B4-7	Aldi (50), fo (50)	−33.2	−30.7	2.0	1.8
B4-8	Aldi (70), spn (30)	−37.9	−30.2	2.5	2.0
B4-9	Aldi (80), spn (20)	−38.6	−35.4	2.3	1.3
A3-4	chondrule en (100)	−10.0	−4.6	2.3	1.6
Leoville AOA-7					
B12-7	Aldi (70), an (30)	−11.6	−13.8	2.6	1.3
B12-8	Aldi (100)	−26.9	−23.0	2.5	1.6
B12-9	fo (100)	−29.0	−28.9	2.3	1.4
Leoville AOA-8					
B11-1	fo (90), Aldi (10)	−36.8	−46.2	2.5	2.0
B11-2	an (100)	−6.8	−0.6	2.6	1.5
B11-3	Aldi (100)	−33.7	−28.8	2.5	1.5
B11-4	Aldi (100)	−35.2	−27.8	2.2	1.3
B11-5	Aldi (100)	−22.6	−18.3	2.3	1.5
B11-6	Aldi (100)	−42.7	−34.3	2.1	1.5
B11-8	fo (95), Aldi (5)	−40.7	−37.0	2.1	1.6
B11-9	fo (100)	−43.9	−39.9	2.4	1.7
B11-10	fo (100)	−37.3	−36.8	2.6	1.8
B12-4	Aldi (80), fo (20)	−20.6	−21.3	2.2	1.4
B12-5	an (100)	−14.4	−9.7	2.2	1.4
B12-6	an (80), Aldi (20)	−10.3	−9.7	2.4	1.5

Table 2. (Continued)

Analysis	Sputtered material (%)	$\delta^{17}O$	$\delta^{18}O$	$1\sigma^{17}O$	$1\sigma^{18}O$
Vigarano AOA-65					
B9-5	Aldi (60), an (30), sp (10)	−34.4	−36.4	2.2	1.8
B9-6	fo (100)	−45.0	−44.1	2.5	1.4
B10-1	fo (100)	−41.4	−31.1	2.6	1.5
B10-2	an (80), Aldi (20)	−43.0	−35.2	2.0	1.5
B10-3	an (50), spn (50)	−41.9	−40.5	2.4	1.6
B13-1	fo (100)	−44.6	−45.3	2.8	2.9
Vigarano AOA-66					
B9-1	fo (95), Aldi (5)	−39.8	−36.4	2.1	1.3
B9-2	fo (100)	−36.7	−36.5	2.4	1.5
B9-3	fo (95), Fe-olv (5)	−41.1	−37.8	2.6	1.6
B9-4	fo (100)	−40.3	−40.3	2.5	1.8
B10-9	Fe-olv (100)	−45.1	−40.9	2.8	1.6
B13-2	fo (100)	−46.6	−45.2	1.8	1.5
B13-3	Fe-olv (75), fo (25)	−42.4	−40.5	2.1	1.6
B13-4	fo (90), Fe-olv (10)	−39.0	−38.3	1.9	1.5
B13-5	fo (80), Fe-olv (20)	−30.1	−27.6	2.8	2.3
B13-6	Fe-olv (60), an (40)	−2.5	9.8	2.4	1.8
Vigarano CAI-67					
B10-4	mel (100)	−26.6	−22.6	2.4	1.7
B10-5	mel (100)	−43.1	−38.7	2.0	1.6
B10-6	mel (100)	−41.0	−36.3	1.9	1.3
B10-7	Aldi (100)	−46.0	−36.3	2.2	1.3
B10-8	Aldi (100)	−44.3	−37.7	2.4	1.6

Abbreviations: an = anorthite; Aldi = Al-diopside; aoa = amoeboid olivine aggregate; di = diopside; fo = forsterite; g.b. = grain boundary; mel = melilite; olv = olivine; spn = spinel.

[a] 1σ calculated as standard deviation of the mean for 60 cycles per analysis.

[b] Elevated ^{16}OH-intensity.

[c] Spot overlapped with troilite inclusion.

[d] Spot overlapped with adjacent FeNi-metal grain.

spinel is enclosed by anorthite near the margins of the CAI-region.

3.2.2. Oxygen Isotopic Analyses

Oxygen isotopic analyses from Leoville AOAs 7 and 8, like results from the Efremovka CAIs, show that forsterite tends to be ^{16}O-rich relative to the other phases (Fig. 6). Forsterite analyses from AOA-8 cluster near −40‰ $\delta^{17,18}O$, but the only forsterite analyzed from AOA-7 plots near −30‰. Al-diopside exhibits a wide range in isotopic composition from −40 to −20‰ $\delta^{17,18}O$. The most ^{16}O-poor results are for anorthite±Al-diopside and fall in a range from ~ −15 to −5‰ $\delta^{17,18}O$, comparable to ^{16}O-poor

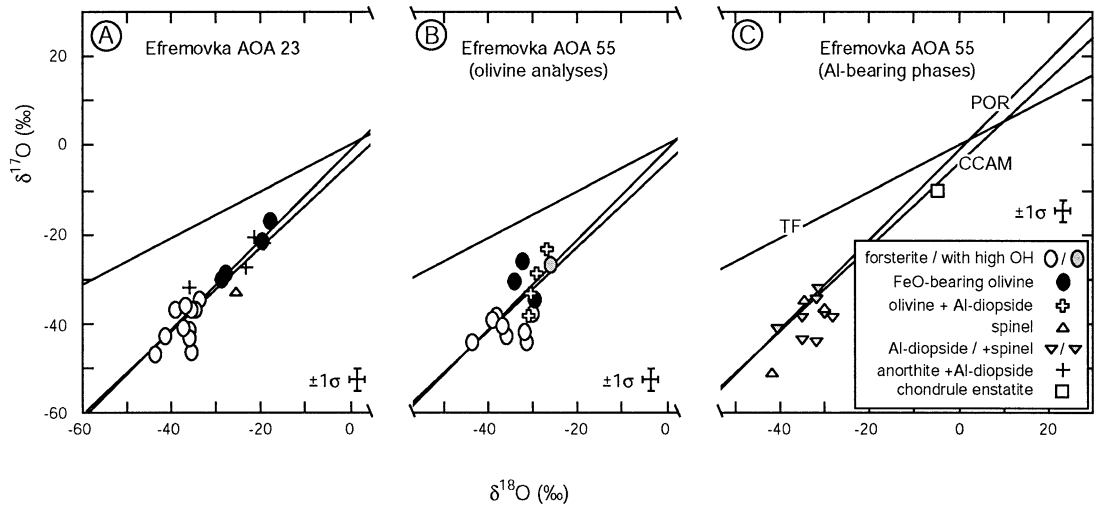

Fig. 3. Oxygen isotopic compositions of minerals analyzed by ion microprobe from Efremovka AOAs 23 and 55 (Table 2). One analysis of enstatite from a chondrule adjacent to AOA-55 is also plotted. Results are normalized to standard mean ocean water (SMOW). Approximate error bars ($\pm 1\sigma$) reflect analytical precision and are shown at right. Reference lines: TF = terrestrial fractionation; CCAM = carbonaceous chondrite anhydrous minerals; POR = primitive oxygen reservoir (Clayton, 1993; Young and Russell, 1998).

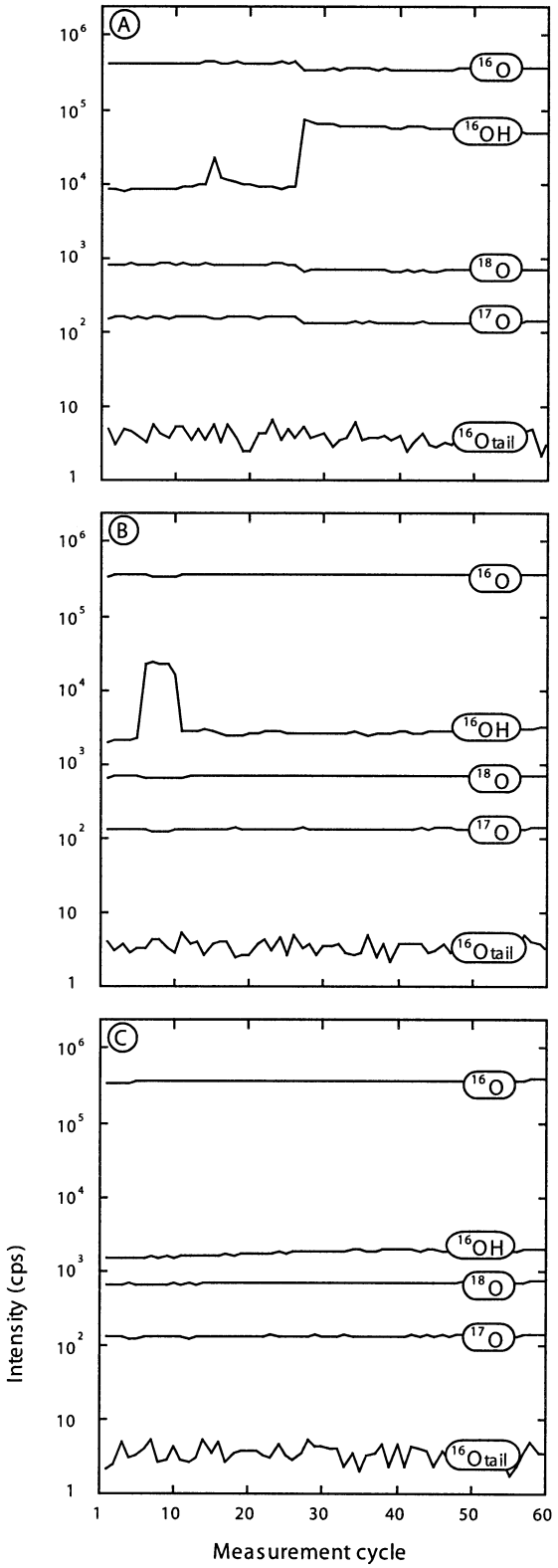

Fig. 4. Signal intensities for ^{16}O, ^{16}OH, ^{18}O, ^{17}O, and "^{16}O-tail" during analyses characterized by: (A) a jump in OH-intensity (analysis A2-2); (B) an abbreviated OH burst (A2-4); and (C) a smooth variation in OH-intensity (A2-6). All three analyses are of olivine and were collected during the same analytical session. Each analysis was collected over approximately 50 min and the intensities have been corrected for detector dead time. Note the log scale.

compositions of some anorthite from coarse-grained CAIs (Clayton, 1993; Yurimoto et al., 1994). All results except for one analysis of forsterite (B11-1; Table 2) fall with 2σ of analytical error of CCAM (Fig. 6); we do not attribute any special significance to the one deviant value.

Unlike the Efremovka analyses, no major jumps in ^{16}OH count rate were detected for Leoville, and no major differences in mean ^{16}OH count rate were detected for consecutive analyses. One analysis of ^{16}O-poor anorthite (B12-5) yielded steplike increases in ^{16}OH-intensity during the analysis, but with count rates increasing only by a factor of $\sim$ 1.5.

3.3. Vigarano AOAs 65 and 66, and Melilite-Pyroxene-Rich CAI-67

3.3.1. Textures and mineralogy

Vigarano AOAs 65 and 66 and melilite-pyroxene-rich CAI-67 occur adjacent to each other (Fig. 7A). AOA-65 is composed of granular forsterite with small FeNi-metal grains and a minor proportion of refractory component. As noted in general for Vigarano AOAs by Komatsu et al. (2001), the olivine in AOA-65 is nearly pure forsterite (Table 1). Unlike the Efremovka AOAs, FeO-enriched grain boundaries of olivine are not characteristic of Vigarano AOA-65 (Fig. 7B). The refractory component consists of Al-diopside enclosing anorthite and spinel. Spinel is minor in abundance and occurs as inclusions in anorthite. Portions of the AOA are mantled by a fine-grained, ferrous olivine-rich accretionary rim.

Vigarano AOA-66 is characterized by more extensive alkali-FeO-alteration than the other AOAs examined in this study. It is composed mostly of olivine with well-developed FeO-rich rims, Al-diopside, and anorthite (Fig. 7C). The interiors of olivine grains have forsteritic compositions, but they are less magnesian than olivine grains from the other AOAs we investigated (Table 1). The olivine rims exhibit a range of compositions as ferrous as Fo_{65}. The rims are only on the order of 1 to 3 μm across, so some of the apparent range in Fo-content may be due to overlap of the electron beam on adjacent magnesian olivine. In contrast to olivine, several analyses of Al-diopside in AOA-66 have MgO/(MgO + FeO) approaching 1.0. Very fine grained, Na-bearing alteration minerals (nepheline?) occur in the interstices between olivine, pyroxene, and anorthite grains and are concentrated near the margins of the AOA. Most of the AOA is surrounded by an olivine-rich accretionary rim. With the textural evidence for alteration, AOA-66 bears a closer resemblance to AOAs from Allende than those from the reduced CVs (Grossman and Steele, 1976; Komatsu et al., 2001).

The melilite-pyroxene-rich CAI-67 is fine-grained; it has a circular general shape in the plane of the thin section, but similar to the AOAs, its surface is characterized by embayments and promontories (Figs. 7A, D). An olivine-rich accretionary rim separates the CAI from Vigarano matrix. The CAI is composed primarily of fine, equant grains of Al-diopside, melilite, and spinel. The Al-diopside occurs in curved mononeralic bands that weave from core to rim of the CAI. Melilite is concentrated in branching domains in the interior and separated from most of the Al-diopside by a thin layer of spinel with tiny inclusions of Al-diopside (Fig. 7D). Spinel

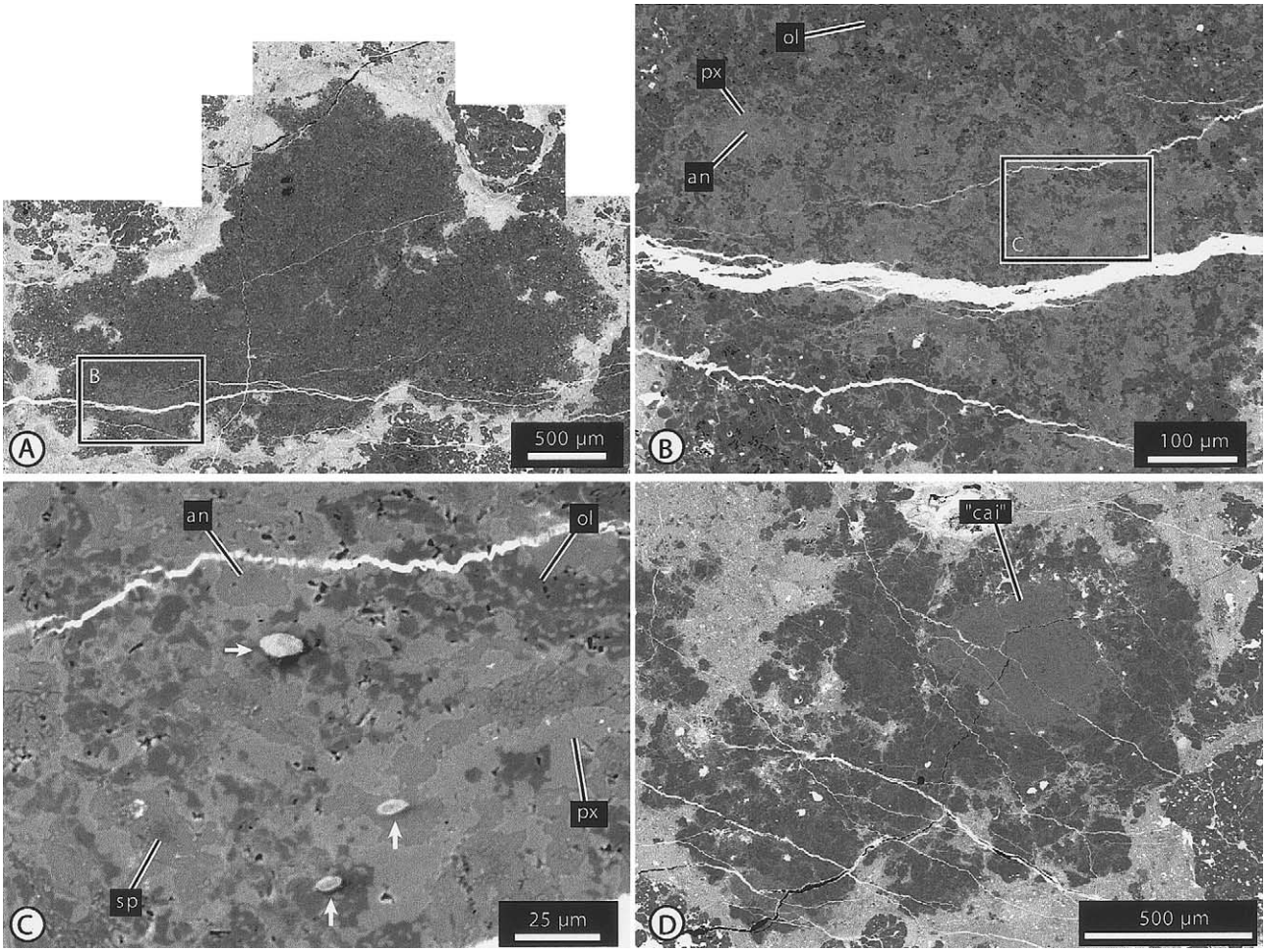

Fig. 5. Electron images of Leoville AOAs 8 (A, B, C) and 7 (D). (A) BSE mosaic of AOA-8. Most of the AOA consists of granular olivine (dark) with an evenly dispersed refractory component of Al-diopside, anorthite, and minor spinel (medium gray). The white veins are from terrestrial weathering. (B) BSE image of a region with a high proportion of the refractory component. (C) Composite BSE/SEI image (see Figs. 2B, C) showing detail of textures and three craters sputtered in the refractory-rich region. Craters are, from top to bottom: B12-4; B11-2; B11-1. (D) BSE image of AOA-7. A region consisting of finely intergrown Al-diopside and anorthite with minor spinel occurs at upper right ("cai"). Bright veins are from terrestrial weathering. Mineral abbreviations as in Figure 1.

crystals free of inclusions commonly occur in the melilite-rich branching domains. Some very fine grained Na-bearing phases are concentrated near the CAI rim.

3.3.2. *Oxygen isotopic analyses*

Analyses from the Vigarano AOAs and CAI-67 show an ^{16}O-rich signal in forsteritic olivine and Al-diopside, and variable ^{16}O-depletions in other phases (Table 2; Fig. 8). Of the three forsterite analyses from AOA-65, two fall on CCAM with $\delta^{17,18}$O between −40 and −45‰, whereas the third (B10-1) is comparable in δ^{17}O, but with a higher value of δ^{18}O, falling to the right of CCAM (Fig. 8A). However, this analysis was collected during session B10, when results appear systematically displaced to the right of CCAM; thus, we suspect that the true composition of the forsterite sputtered in B10-1 is closer to CCAM. The other analyses from AOA-65 include ^{16}O-rich mixtures of anorthite+Al-diopside and anorthite+spinel, and one slightly ^{16}O-depleted composition from Al-diopside+anorthite+spinel (Table 2; Fig. 8A).

Forsteritic olivine from AOA-66 is more FeO-rich than the AOA-65 forsterite (Table 1), but most isotopic analyses from AOA-66 are ^{16}O-rich, comparable to those of AOA-65 (Table 2; Fig. 8B). However, the AOA-66 forsterites do exhibit a trend toward more ^{16}O-depleted compositions, including one analysis yielding $\delta^{17,18}$O ∼ −30‰. Two analyses of FeO-rich olivine are similar in isotopic composition to the ^{16}O-rich forsteritic olivine; however, one analysis of a FeO-rich olivine+anorthite mixture (B13-6) is ^{16}O-poor, near 0‰ $\delta^{17,18}$O. The ^{16}O-depleted forsterite (B13-5) and ^{16}O-poor olivine+anorthite (B13-6) analyses yielded ^{16}OH count rates higher than preceding analyses by factors of approximately two and three, respectively.

The analyses of Al-diopside and two of three analyses of melilite from CAI-67 are ^{16}O-rich, with $\delta^{17,18}$O near −40‰ (Table 2; Fig. 8C). The other melilite analysis (B10-4) overlaps

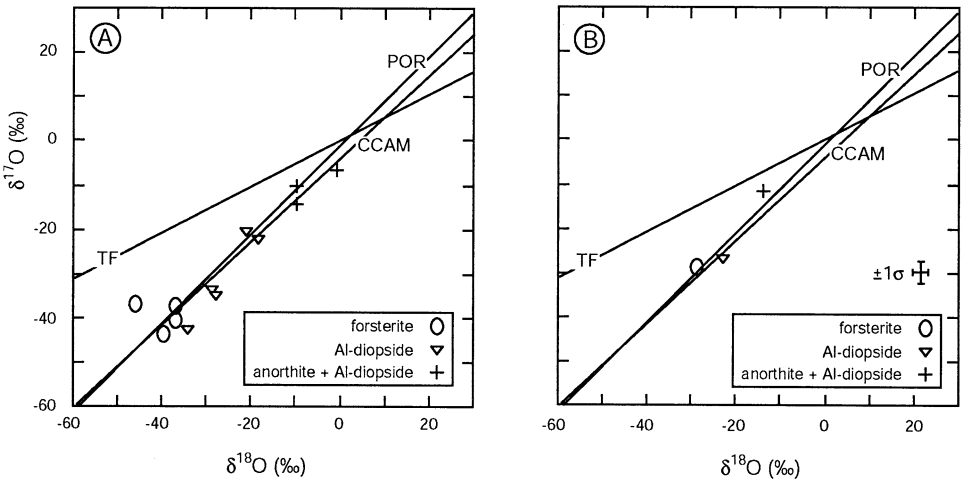

Fig. 6. Oxygen isotopic compositions of minerals analyzed by ion microprobe from Leoville AOAs 8 (A) and 7 (B). Normalization, approximate error bars, and reference lines as in Figure 3.

with a crack (Fig. 7D) and is relatively depleted in ^{16}O, with $\delta^{17,18}O$ near −20‰. The ^{16}O-depleted melilite is less gehlenitic than the ^{16}O-rich melilites ($Åk_{36}$ vs. $Åk_{14}$ and $Åk_{19}$; Table 1). Count rates of ^{16}OH for the ^{16}O-depleted melilite were approximately five to six times greater than for the ^{16}O-rich melilite analyses, which were collected in sequence during the same analytical session (Fig. 9). All of these results fall slightly to the right of CCAM (Fig. 8C), but they were collected during a single analytical session, B10, which, as noted above, was characterized by results consistently ^{18}O-rich relative to CCAM. Most of the results from CAI-67 are within 2σ analytical precision of CCAM, and we do not infer that CAI-67 phases are fractionated significantly from CCAM-like compositions.

4. DISCUSSION

4.1. Multistage Evolution of AOAs: Evidence from Mineralogy and Textures

Textures and elemental compositions of minerals from the AOAs studied here reflect an early stage of petrogenesis involving moderately refractory elements followed by variable alteration resulting in an enrichment in volatile components (Komatsu et al., 2001). This broad petrogenetic framework is appropriate for many AOAs, as it is consistent with results from Allende (Grossman and Steele, 1976; Kornacki and Wood, 1984), COs (Chizmadia et al., 2002), and the large set of AOAs from reduced CVs examined by Komatsu et al. (2001). However, different studies have favored nebular (Grossman and Steele, 1976; Hashimoto and Grossman, 1987) vs. parent body (Komatsu et al., 2001; Chizmadia et al., 2002; Imai and Yurimoto, 2003) settings for the low-temperature stage.

These previous studies and our own results indicate that the early, high-temperature stage involved condensation and growth of granular grains of forsterite ~ 5–15 μm in diameter. Composite nuggets of finer-grained Al-diopside, anorthite, and spinel also formed and came into contact with strands and clumps of grains of forsterite. Isolated grains of FeNi-metal comprised a widespread but relatively minor 1st-generation component of the AOAs. This similarity in condensation temperatures of FeNi-metal, olivine, diopside, and spinel (Grossman, 1972; Petaev and Wood, 1998; Ebel and Grossman, 2000) suggests that the 1st-generation mineral assemblages of AOAs were sensitive to volatility. The aggregates became lithified during sintering and localized melting and recrystallization along grain boundaries (Komatsu et al., 2001). The amoeboidal shapes and the absence of classical igneous textures indicate that the proportion of melting on the "whole-rock" scale remained low. However, localized melting along forsterite-anorthite grain boundaries and crystallization of Al-diopside (Komatsu et al., 2002) may account in part for the textural sequence of olivine, Al-diopside, anorthite, and spinel in the refractory domains (Figs. 1, 5, and 6). The branching texture in Efremovka AOA-55 differs from the more common, equant refractory nodules, yet even in the branching textural domains, olivine grains are separated from spinel by an intervening layer of Al-diopside (Fig. 2B). These branching domains may have undergone a higher proportion of melting than the granular domains.

Textural and compositional evidence of alteration is variable among the AOAs we examined. The least altered AOA in this study is Vigarano AOA-65. The olivine in this AOA is nearly pure forsterite (Table 1), with no evidence for FeO-enrichment along olivine grain boundaries or interstitial Na-bearing alteration phases (Fig. 7B). Ironically, the most heavily altered AOA, Vigarano AOA-66, occurs adjacent to AOA-65 in Vigarano. Even the most forsteritic cores of olivine grains analyzed from AOA-66 have significant FeO, and all of the forsteritic cores are surrounded by FeO-rich rims, with Fo-contents ranging at least as low as Fo_{69} (Table 1; Fig. 7C). Very fine-grained, interstitial, Na-bearing alteration phases are concentrated in peripheral zones of the AOA, but occur in much of the interior as well. Due to the fine grain size, we have not identified the mineralogy associated with sodic alteration. Nonetheless, the abundance of Na-bearing phases combined with the zoned FeO-rich olivine grains indicate that AOA-66 was altered at temperatures low enough to permit stability of FeO-rich olivine and condensation of Na-bearing phases.

The other AOAs record intermediate stages of textural alter-

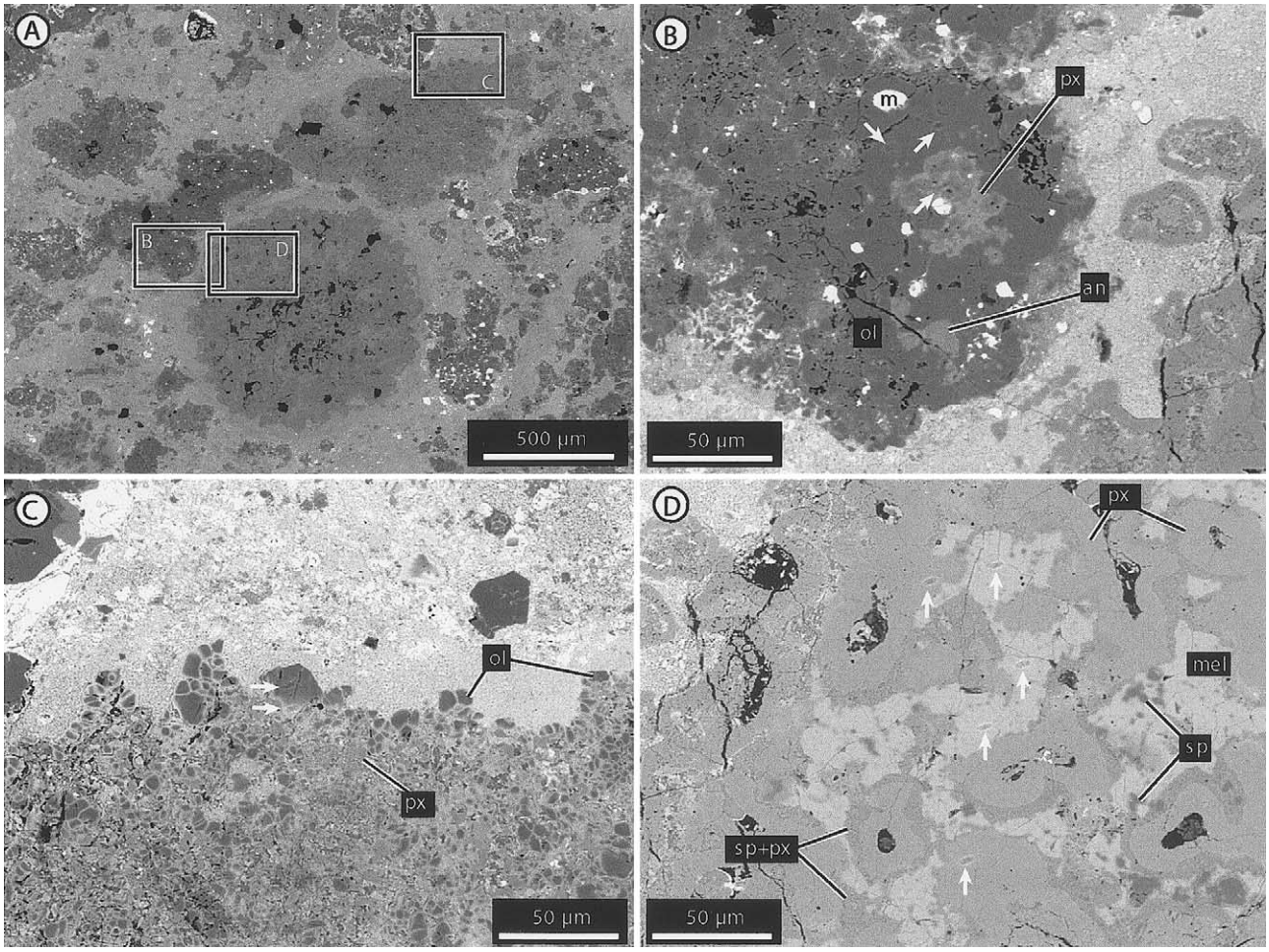

Fig. 7. BSE images of Vigarano AOAs 65 and 66, and fine-grained, melilite-pyroxene-rich Ca-Al-rich inclusion, CAI-67. (A) CAI-67 is the spherical object at center; AOA-65 is located above and to the left of the CAI; AOA-66 is located in the upper right portion of the image. The darker appearance of AOA-65 compared to AOA-66 reflects the more Fo-rich composition of olivine grains in the former. (B) Detail of AOA-65, showing an olivine "doughnut" around a refractory domain composed of Al-diopside, anorthite, and spinel. White grains are FeNi metal. Craters sputtered during SIMS analyses consist of B13-1 (upper left); B10-1 (upper right); and B10-3 (center). (C) Detail of AOA-66, showing forsteritic olivine grains rimmed by fayalitic olivine, and abundant Al-diopside in the interior. Sputtered craters at center are: B9-4 (upper); B10-9 (lower). (D) Detail of CAI-67, showing crystal boundaries of melilite, Al-diopside, and spinel. Dark to medium gray zones separating melilite (mel) from most Al-diopside are fine-grained mixtures of spinel and Al-diopside (sp+px). Craters sputtered during SIMS analyses are, from top to bottom: B10-4; B10-7; B10-6; B10-5; B10-8. Mineral abbreviations as in Figure 1.

ation between the extremes of AOAs 65 and 66 from Vigarano. Efremovka AOA-23 and the granular domain of AOA-55 have olivine grains with nearly pure forsterite interiors and somewhat diffuse FeO-enriched zones along olivine-olivine grain boundaries (Table 1; Fig. 1B). Spinel in the branching domain of AOA-55 is rarely associated with a fine-grained, FeO-rich alteration phase. Most of the opaque grains in the Efremovka AOAs consist of FeNi-metal, but some troilite is also present, suggesting a stage of limited crystallization or alteration below troilite condensation temperatures near 700K (Petaev and Wood, 1998). Fine-grained sodic and FeO-rich alteration phases are present in Leoville AOAs 30 and 75, but are rare. Likewise, Vigarano CAI-67 is characterized by some fine-grained sodic alteration near its rim, but does not exhibit the pervasive evidence of alteration of Vigarano AOA-66.

4.2. Diffusion Modeling: What Were the Timescales and Mechanisms of AOA Alteration?

4.2.1. Model constraints and calculations

Petrographic, elemental, and isotopic results show that AOAs in the reduced CVs were originally FeO-poor and ^{16}O-rich. Some of the AOAs were modified subsequently, showing variable depletions in ^{16}O and enrichments in FeO in olivine. If alteration was controlled by diffusion, then mineral compositions should match predictable patterns based on the knowledge of grain shapes, dimensions, diffusion parameters, and compositions of the initial grains and the gas or fluid environment in which alteration took place. Further, if such a match is obtained, then it may be possible to make quantitative estimates of timescales or cooling rates of alteration.

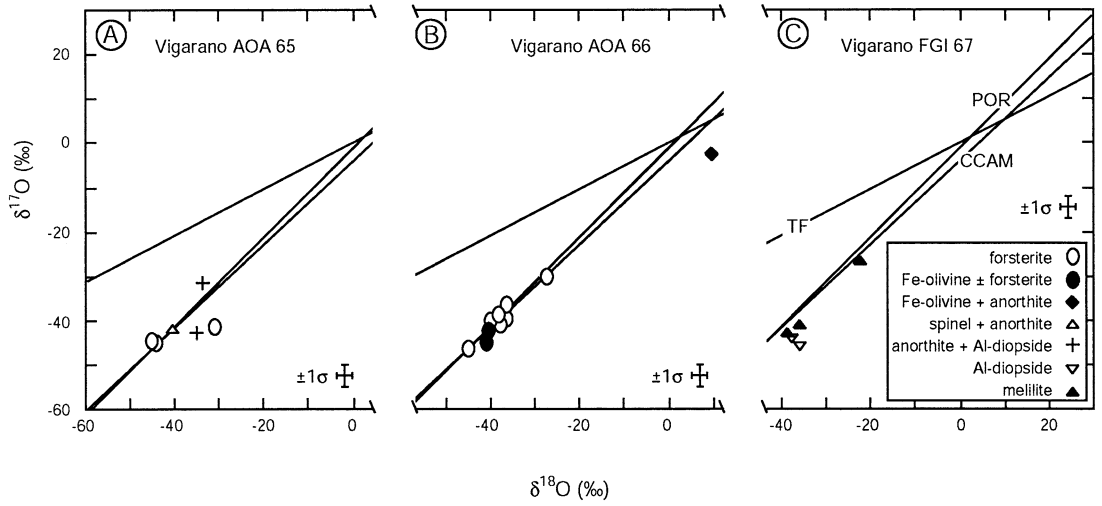

Fig. 8. Oxygen isotopic compositions of minerals analyzed by ion microprobe from Vigarano AOAs 65 (A) and 66 (B), and CAI-67. Normalization, approximate error bars, and reference lines as in Figure 3.

In the following treatment of diffusion, we assume that 1st-generation minerals in AOAs were: (1) spherical; (2) ^{16}O-rich; (3) FeO-poor; and (4) homogeneous in composition. Spherical grain-shape is obviously a simplification, but all the major AOA primary minerals are equant rather than elongate or sheetlike, so a spherical approximation is appropriate for modeling. The ^{16}O-rich, FeO-poor initial compositions are based on observations of AOA minerals from mineralogically unaltered chondrites (e.g., Aléon et al., 2002; Chizmadia et al., 2002; Itoh et al., 2002; Fagan et al., 2003), and thermodynamic models that predict that initial silicates and oxides condensing from gases originating from a variety of physical conditions are FeO-poor (Grossman, 1972; Petaev and Wood, 1998; Ebel and Grossman, 2000; however, see Grossman and Fedkin, 2003).

From these initial conditions, diffusive reequilibration of spherical grains in a surrounding environment of fixed composition results in a series of predictable zoning profiles as time progresses (Fig. 10). Figure 10 is based on the work of Crank (1975; see his fig. 6.1), who uses fixed values of Dt/a^2 (where D = diffusion coefficient, t = time, and a = grain radius) for each compositional profile, whereas we use values of fractional equilibration, f:

$$f = 1 - \frac{6}{\pi^2}\sum_{n=1}^{\infty}\frac{1}{n^2}\exp\left[-n^2\pi^2\left(\frac{Dt}{a^2}\right)\right] \quad (1)$$

Values of f range from f = 0 for absence of diffusion to f = 1 for complete equilibration by diffusion. Intermediate values correspond to specific zoning profiles (Fig. 10).

For a given zoning profile, a set of temperature-time and temperature-cooling rate solutions can be calculated if diffusion parameters and grain radii are known. In this study, we use a 6-μm radius for olivine and 2-μm radii for anorthite, Al-diopside, and spinel. These grain sizes are somewhat larger than the mean radii observed in thin section, but most of our isotopic analyses are from coarser than average grains. We note further that mean radii of equant grains in thin section appear finer than true radii because the section surface shows many off-center slices through grains.

Estimates of the key diffusion parameters, frequency factor D_o and activation energy Q, are available from experimental studies, and are used to calculate the diffusion coefficient D over a range of temperatures from:

$$D = D_o e^{(-Q/RT)} \quad (2)$$

Frequency factors and activation energies have been determined from experimental studies of single crystals of synthetic forsterite by Jaoul et al. (1983; Table 3; also see Jaoul et al., 1980; Reddy et al., 1980). Diffusion rates in olivine are expected to increase with both Fa-content and oxygen fugacity (fO_2), as these conditions lead to perturbations in olivine stoichiometry that, although minor in elemental composition, are significant in contributing to the concentration of crystalline defects (Nakamura and Schmalzried, 1983). However, for olivines over the range $Fo_{\sim 85\text{-}100}$, diffusion rates of oxygen (Jaoul et al., 1983; Gérard and Jaoul, 1989; Ryerson et al., 1989) and Fe-Mg (Chakraborty, 1997) do not show a strong sensitivity to composition.

We use two types of thermal models, analogous to two of the model histories examined by Ryerson and McKeegan (1994): (1) heating at a fixed temperature for a specified time; and (2) instantaneous heating to an initial temperature, T_0, followed by cooling from a specific initial cooling rate. Both models are simpler than natural thermal histories; however, the goal of the modeling is not to duplicate natural events, but to evaluate whether diffusion is a plausible mechanism of alteration. Fractional equilibration as a function of time can be calculated for fixed-temperature heating by simple application of Eqns. 1 and 2. Modeling diffusion during cooling requires an integral solution to sum incremental changes in composition as temperature drops from the initial temperature, T_0. We adopt the approach of Ryerson and McKeegan (1994) and use a solution developed by Kaiser and Wasserburg (1983) for the time-integral, $\tau(\infty)$, of the diffusion coefficient for temperature drop-

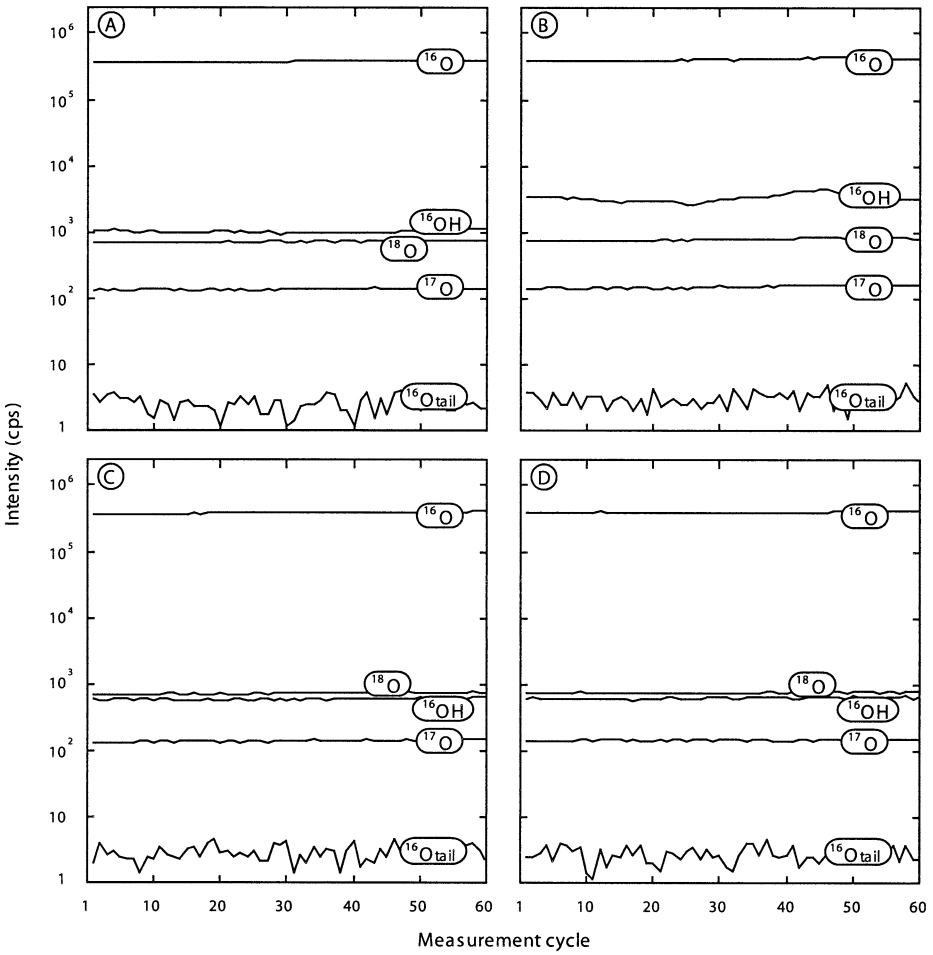

Fig. 9. Comparison of ^{16}OH-intensities from SIMS analyses of AOA-65 and CAI-67 from Vigarano. Signal intensities of ^{16}O, ^{16}OH, ^{18}O, ^{17}O, and "^{16}O-tail" are plotted for analyses collected in sequence during the same analytical session: (A) analysis B10-3 of a mixture of ^{16}O-rich anorthite+spinel from a refractory nodule in AOA-65; (B) analysis B10-4 of melilite ($Åk_{36}$) from CAI-67 with ^{16}O-depleted composition; (C) analysis B10-5 of ^{16}O-rich melilite ($Åk_{14}$) from CAI-67; (D) analysis B10-6 of ^{16}O-rich melilite ($Åk_{19}$) from CAI-67. See Table 2 for isotopic results and Figure 7D for locations of the melilite analyses. Signal intensities are corrected for dead time. Note the log scale.

ping from T_0 to the temperature at which the diffusion rate approaches zero:

$$\tau(\infty) \cong \frac{RT_0^2 D(T_0)}{r_0 Q} \quad (3)$$

where R is the gas constant, $D(T_0)$ is the diffusion coefficient at T_0, Q is the activation energy (Eqn. 2), and r_0 is the initial cooling rate. We then substitute $\tau(\infty)$ for Dt in Eqn. 1 to determine f for a cooling system. Model results were calculated using routines written in MATLAB by the senior author.

Our oxygen isotopic results for olivine are compared with Fo-content and with oxygen isotopic compositions of coexisting Al-diopside, anorthite and spinel. For Fe-Mg diffusion, we use parameters from the recent study of Chakraborty (1997; Table 3), which covers the compositional range of interest and was determined at relevant fO_2 (10^{-12} bars). We recognize that significant controversy exists over the true Fe-Mg diffusion rates in olivine (Buening and Buseck, 1973; Misener, 1974; Jurewicz and Watson, 1988; Chakraborty et al., 1994; Miyamoto et al., 2002). The Chakraborty (1997) study yields the slowest Fe-Mg diffusion rates in olivine, but these are still faster by two orders of magnitude or more than oxygen (Fig. 11).

Oxygen diffusion parameters for spinel, anorthite and diopside were analyzed by Ryerson and McKeegan (1994). The Ryerson and McKeegan results for spinel are similar to those of previous studies (Reddy and Cooper, 1981; Ando and Oishi, 1983) and are used here. Their results for anorthite [010] fall near those of Elphick et al. (1988) for the [001] direction. For their modeling, Ryerson and McKeegan derived parameters based on both their and the Elphick et al. results, and we do the same in this study. Oxygen diffusion in diopside was evaluated by Ingrin et al. (2001) in a study that yielded values of D comparable to the Ryerson and McKeegan results over ~ 1100 to 1300°C, but predicted faster rates of diffusion at lower temperatures as a consequence of a lower activation energy (Table 3; Fig. 11). For the present study, we consider both the Ryerson and McKeegan (1994) and Ingrin et al. (2001) calibrations.

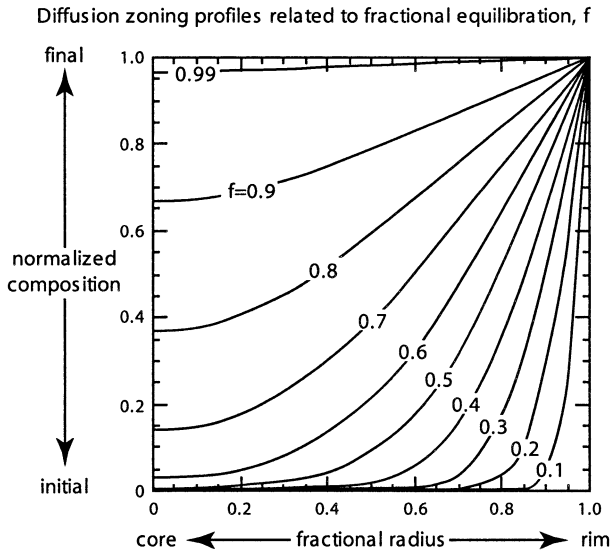

Fig. 10. Diffusion-controlled zoning profiles for fixed values of fractional equilibration, f, in a spherical grain (see fig. 6.1 of Crank, 1975). Fractional radius is calculated from r/a, where r = distance from core and a = grain radius. Normalized composition is calculated from $(C-C_1)/(C_0-C_1)$, where C = composition, C_0 = surface composition, C_1 = initial composition of grain. See Eqn. 1 for definition of fractional equilibration, f. Note that alteration of a grain core by diffusion requires $f \geq \sim 0.6$.

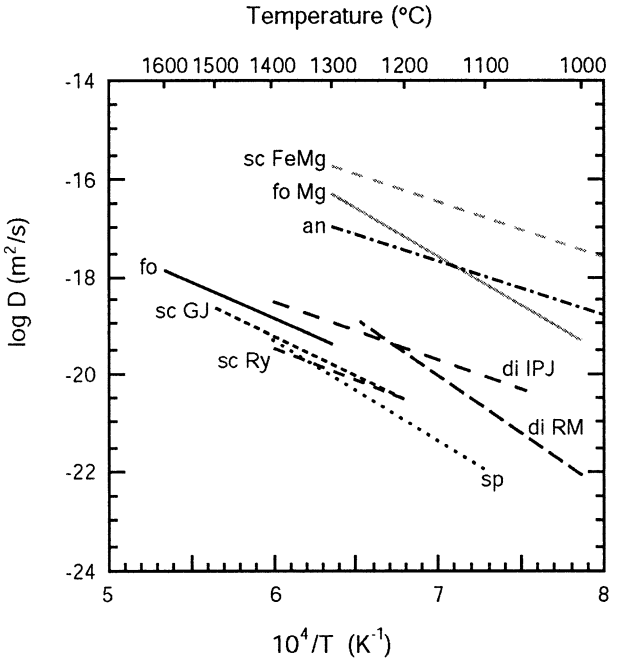

Fig. 11. Diffusion coefficients and temperature ranges of experimental calibration for minerals in reduced CV AOAs. Oxygen diffusion parameters are from the following studies: an, anorthite (combined calibration of Elphick et al., 1988, and Ryerson and McKeegan, 1994); di RM, diopside (Ryerson and McKeegan, 1994); di IPJ, diopside (Ingrin et al., 2001); fo, forsterite (Jaoul et al., 1983); sc GJ, San Carlos olivine (Fo_{90}, Gérard and Jaoul, 1989); sc Ry, San Carlos olivine (Fo_{92}, Ryerson et al., 1989); sp, spinel (Ryerson and McKeegan, 1994). Cation diffusion coefficients are: sc FeMg, Fe-Mg interdiffusion in San Carlos olivine (Fo_{86}, Chakraborty, 1997); fo Mg, Mg diffusion in forsterite (Chakraborty et al., 1994).

4.2.2. *Results of diffusion modeling*

Modeling results for constant-temperature heating are presented in Figure 12. Figure 12A shows the temperature-time combinations for oxygen diffusion in olivine (Fo_{100}, grain radius = 6 μm) to attain fractional equilibration values of f = 0.1, 0.3, 0.7 and 0.9. The temperature-time combinations for Fe-Mg diffusion in olivine (Fo_{86}) to attain f = 0.1, 0.6, and 0.99 are also shown, although these solutions show time maxima because diffusion rate increases as Fa-content increases. Nonetheless, the plotted results highlight the different diffusion rates of O vs. Fe-Mg in olivine. As a consequence of these different rates, simultaneous diffusion of Fe and isotopically distinct O into forsterite does not result in a correlation between Fo-content and oxygen isotopic composition in zoned grains. Instead, by the time an olivine grain has undergone minor exchange of O ($f_O \sim 0.1$), the grain has completely equilibrated with respect to Fe ($f_{FeMg} \sim 1.0$; Fig. 12A). This pattern is expected to hold even for large increases in Fa-content, because the higher concentrations of defects associated with fayalitic olivine should result in higher diffusion rates for both Fe-Mg and O (Nakamura and Schmalzried, 1983; Gérard and Jaoul, 1989; Chakraborty, 1997). Thus, olivine that has undergone partial Fe-Mg-equilibration should retain its original oxygen isotopic composition if compositional exchange is controlled by diffusion. This is also true for model diffusion during cooling (Fig. 13A).

Table 3. Parameters used for modeling diffusion in AOAs[a].

	D_o (m^2/s)[b]	Q (kJ/mol)[b]
O in forsterite[1]	2.3×10^{-10}	293
O in anorthite[2,3,c]	1.5×10^{-10}	217
O in diopside[3]	4.3×10^{-4}	457
O in spinel[3]	2.2×10^{-7}	404
O in diopside[4]	2.0×10^{-11}	234
Fe-Mg in olivine[5]	5.4×10^{-9}	226

[a] Data sources: [1]Jaoul et al. (1983); [2]Elphick et al. (1988); [3]Ryerson and McKeegan (1994); [4]Ingrin et al. (2001); [5]Chakraborty (1997).
[b] See Eqn. 2 for parameter definitions.
[c] Anorthite parameters from combined experimental results.

Modeling also shows that minor oxygen isotopic exchange ($f \sim 0.1$) in AOA forsterite can occur by diffusion within the temperature-time limits of the solar nebula. A forsterite grain with 6 μm radius attains a fractional equilibration value of f = 0.1 if oxygen diffusion proceeds at 900°C for 55 yr, or at 1100°C for 250 d (Fig. 12A). The same zoning pattern can be attained by cooling from 900°C at an initial rate of 0.04°C/yr, or from 1100°C at an initial rate of 4.3°C/yr (Fig. 13A). These rates are much slower than estimates for chondrule and igneous CAI cooling, although chondrule and CAI cooling rates cover a higher temperature range (Jones et al., 2000). Faster cooling rates and shorter heating durations are plausible for higher temperatures, but higher temperatures also lead to evaporation of AOA minerals under a range of pressures and dust:gas ratios (e.g., Ebel and Grossman, 2000). In fact, specific conditions of low pressure (10^{-6} bars) and low dust:gas (1:1) result in

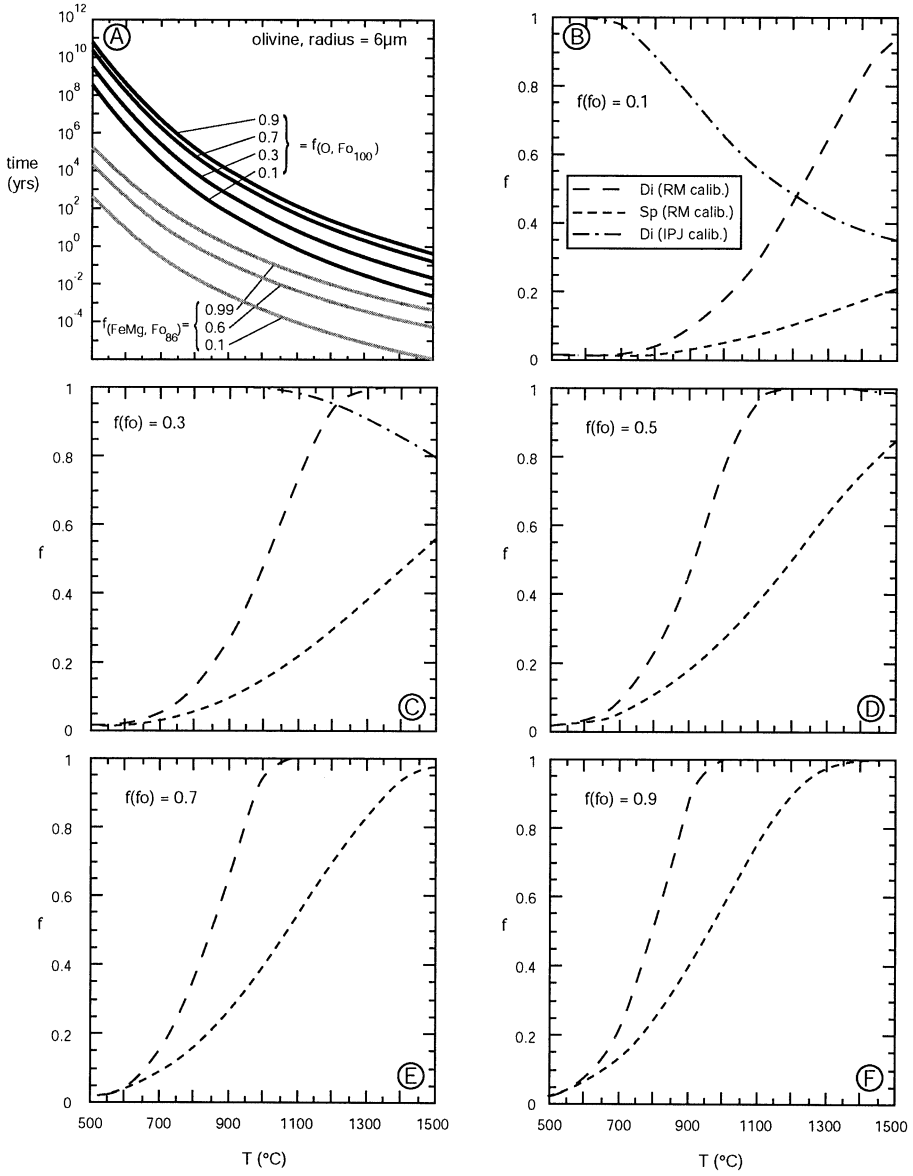

Fig. 12. Fractional equilibration, f, in model minerals resulting from diffusion at constant temperature. (A) Time required for olivine to attain noted values of f as a function of temperature. Time-temperature curves are shown for oxygen diffusion in forsterite and Fe-Mg diffusion in Fo_{86}. (B) Values of f for oxygen diffusion in diopside and spinel coexisting with forsterite with f = 0.1. Temperatures are fixed explicitly on the horizontal axis, and heating time is also fixed at each temperature by the requirement that f = 0.1 for oxygen diffusion in forsterite. Curves are based on diffusion calibrations of Ryerson and McKeegan (RM) for spinel and diopside, and Ingrin et al. (IPJ) for diopside (Table 3). See text for discussion of the differences between the RM and IPJ calibrations for diopside. Model anorthite has fully equilibrated (f = 1) with the surrounding oxygen reservoir. (C-F) Analogous to (B) with forsterite f = 0.3, 0.5, 0.7 and 0.9. Model grains are spherical with radii of 6 μm for olivine and 2 μm for anorthite, diopside and spinel. Zoning profiles for spherical grains of specified f are shown in Figure 10.

evaporation of AOA minerals at temperatures slightly below 1000°C (Ebel and Grossman, 2000).

Heating in the reduced CV parent body may not have been of sufficient temperature or duration to cause significant oxygen isotopic exchange in AOA olivine by diffusion. Minor oxygen isotopic exchange (f = 0.1) in model forsterite can be attained by heating at 500°C for over 10^8 yr or at 600°C for $\sim 10^6$ yr (Fig. 12A). It is not clear if the reduced CV chondrites were metamorphosed under these conditions (Guimon et al., 1995; Lee et al., 1996; Krot et al., 1998). On the other hand parent body heating may have been strong enough to cause diffusive exchange of Fe and Mg in olivine (Weinbruch et al., 1994).

Oxygen isotopic compositions resulting from diffusion in coexisting forsterite (radius = 6 μm), diopside and spinel (radii = 2 μm) are shown in Figures 12B–F for heating at constant temperature. In each of these panels, fractional equilibration for oxygen diffusion in olivine is fixed; therefore, the heating duration, t, at a given temperature, T, is also fixed. These panels relate temperature

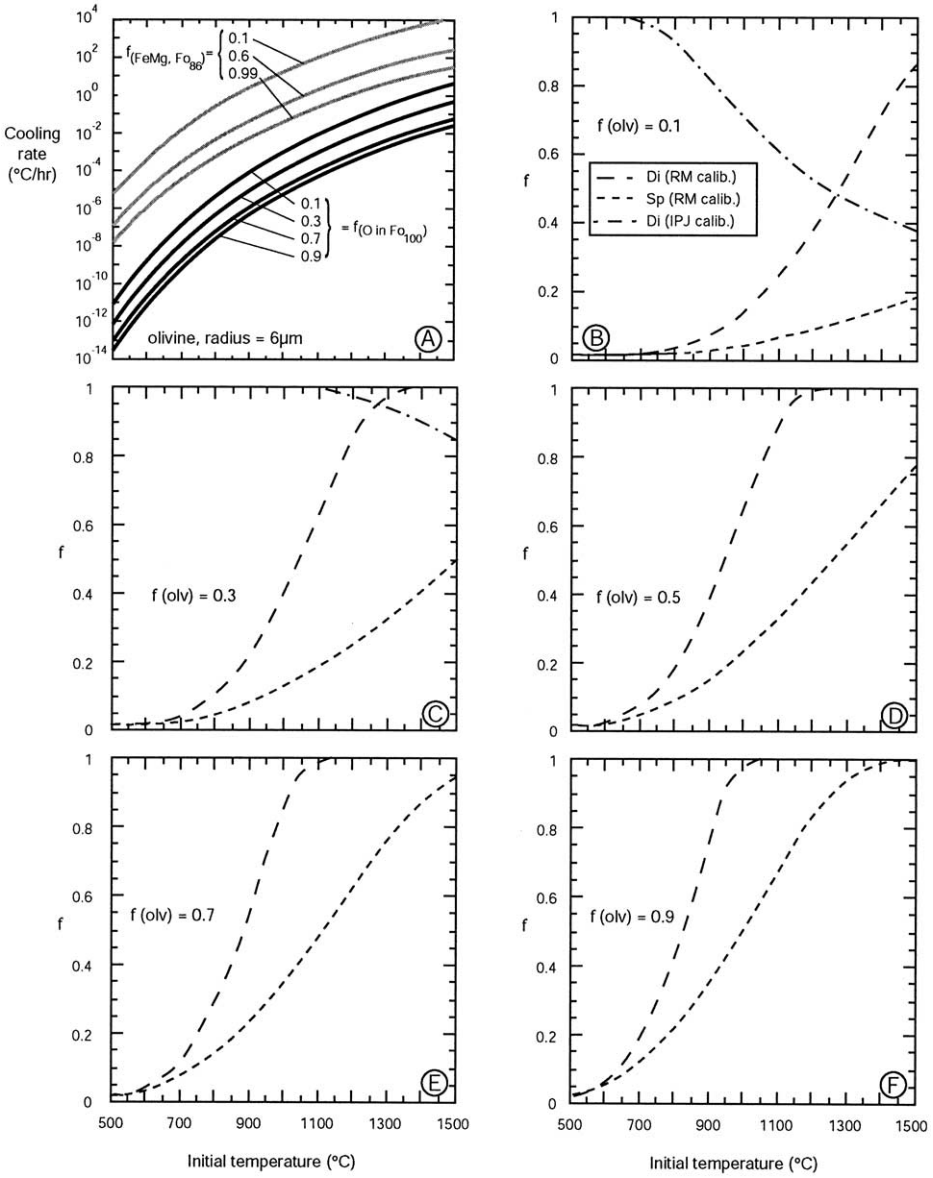

Fig. 13. Fractional equilibration, f, in model minerals resulting from diffusion as temperature drops at a specific initial rate from an initial temperature. (A) Initial cooling rate required for olivine to attain noted values of f as a function of initial temperature (see Eqn. 3). Curves of initial cooling rate vs. initial temperature shown for oxygen diffusion in forsterite and Fe-Mg diffusion in Fo_{86}. (B) Values of f for oxygen diffusion in diopside and spinel coexisting with forsterite with f = 0.1. Initial temperatures are fixed explicitly on the horizontal axis, and initial cooling rate is also fixed at each temperature by the requirement that f = 0.1 for oxygen diffusion in forsterite. Anorthite has fully exchanged (f = 1) with the surrounding oxygen reservoir. (C-F) Analogous to (B) with forsterite f = 0.3, 0.5, 0.7 and 0.9. Model grain shapes and diffusion parameters are the same as in Figure 12. See text for discussion of the differences between the Ryerson and McKeegan (1994, "RM") and Ingrin et al. (2001, "IPJ") calibrations for diopside.

and time to fractional equilibration in diopside and spinel (radii = 2 μm). Model spinel exhibits minor to negligible diffusive equilibration at all temperatures below 1100°C for olivine that has also undergone minor exchange (Fig. 12B). As heating duration increases, spinel undergoes greater equilibration at relatively high temperatures, but fractional equilibration resulting from low-temperature, long-term heating remains low (Figs. 12C–F). The Ryerson and McKeegan (1994, "RM" in this discussion) and Ingrin et al. (2001, "IPJ") calibrations yield many conflicting predictions for diopside. Under long-term, low-temperature (<800°C) conditions that lead to minor isotopic exchange in forsterite, the RM calibration predicts that diopside undergoes minimal isotopic exchange, whereas the IPJ calibration predicts that diopside undergoes nearly complete isotopic exchange (Fig. 12B). However, under shorter-term, higher-temperature (900°C<T<1400°) conditions, the two calibrations are similar in that they both predict intermediate oxygen exchange in diopside. As heating duration increases, the IPJ calibration predicts that fractional equilibration is complete or nearly complete in model diopside for both high- and low-temperature events (Figs. 12C–F). The RM calibration

predicts similar, extensive equilibration at high temperatures, but minor equilibration at low temperatures. Model anorthite (radius = 2 μm) has fully exchanged oxygen with the surrounding environment at all temperature-time histories considered. Similar patterns of oxygen isotopic exchange in model AOA minerals are obtained for diffusion during cooling, indicating that these patterns do not depend on constant temperature heating (Figs. 13B–F).

4.2.3. Comparison of model with observed results

4.2.3.1. Efremovka AOAs 23 and 55. Most olivine grains from Efremovka AOAs 23 and 55 have forsteritic ^{16}O-rich cores, and FeO-rich ^{16}O-depleted rims (Fig. 3). This correlation between Fo-content and oxygen isotopic composition is very difficult to reconcile with alteration by diffusion because Fe and Mg diffuse much more rapidly in olivine than O (Figs. 12A and 13A). It is possible that the correlation between oxygen isotopic composition and Fo-content was caused by an early diffusive exchange of oxygen isotopes followed by diffusion from a FeO-rich reservoir; however, this requires that the correlation is simply a coincidence resulting from a fortuitous combination of two separate diffusion events. Furthermore, compositional exchange by diffusion is not supported by the oxygen isotopic compositions of anorthite from Efremovka AOA-23. These analyses were affected by beam overlap with adjacent Al-diopside; nonetheless, the available results do not indicate that the anorthite completely exchanged oxygen, contradicting model predictions (Figs. 12 and 13).

Another possibility is that the concentrations of Fe^{2+} dissolved in local aqueous fluids varied during hydrothermal metamorphism on the Efremovka parent body, possibly as consequence of a vapor to liquid phase transition of aqueous fluid. Under this scenario, the Efremovka AOAs might have been in contact continuously with ^{16}O-poor fluid that was enriched at a late stage in dissolved Fe^{2+}. The contrast in AOA-55 between ^{16}O-depleted, FeO-poor olivine rims in the branching textural domain and ^{16}O-depleted, FeO-rich olivine rims in the granular domain may have resulted from a variation in original porosity: a higher percentage of melting and recrystallization may have resulted in a less permeable structure in the branching domain. Continuous exposure to ^{16}O-poor fluid or vapor may have caused ^{16}O-depletion of olivine grain boundaries, whereas a late-stage enrichment in dissolved Fe^{2+} was of insufficient duration to penetrate the low-porosity branching domains and cause significant Fe-Mg exchange in olivine.

Alternatively, it is possible that FeO-enrichment and ^{16}O-depletion in the AOA olivine rims were controlled by a mechanism other than diffusion. Compositional exchange in the olivine rims may have occurred by dissolution and reprecipitation, possibly followed by a relatively dry thermal pulse, similar to the sequence of events proposed for parent body alteration in CV chondrites (Kojima et al., 1993; Krot et al., 1995, 1998; Kojima and Tomeoka, 1996; Imai and Yurimoto, 2003). As discussed by these authors, after partial dissolution of the preexisting olivine, another mineral, perhaps a phyllosilicate, may be precipitated and then transformed to fayalitic olivine during subsequent metamorphism. However, this multistage alteration and dehydration should produce oxygen isotopic fractionations in addition to simple mixing (Clayton and Mayeda, 1999). Alternatively, olivine may have precipitated directly from fluid; though conditions for olivine precipitation remain to be verified experimentally. The presence of an aqueous phase during alteration of the olivine is supported by high levels of ^{16}OH detected during some analyses of some relatively ^{16}O-poor olivine (Fig. 4.).

Yet another set of factors that could enhance isotopic exchange on the Efremovka parent body are the possible effects of deformation. Deformation may have been driven by hydrofracturing as ices expanded during melting and vaporization (Wilson et al., 1999) and by shock deformation during asteroidal impacts (Scott et al., 1992; MacPherson and Krot, 2002). These processes are difficult to address, but they would be expected to enhance the ingress of fluids into AOAs and increase diffusion rates by deformation of crystal structures.

4.2.3.2. Leoville AOAs 7 and 8. In contrast to the Efremovka AOAs, Leoville AOAs 7 and 8 have oxygen isotopic systematics that may be explained as a consequence of variable rates of diffusion in AOA minerals. Isotopic analyses indicate that olivine in these AOAs has experienced only minor oxygen isotopic exchange, whereas feldspar has undergone extensive exchange and diopside yields a range of isotopic compositions indicating fractional exchange (Fig. 6). Assuming fractional exchange in olivine of f $\sim$ 0.1, then extensive zoning (f = 0.1 to 0.8; Fig. 10) in diopside is attained simultaneously with complete isotopic equilibration in anorthite under constant temperature heating at $\sim$ 900 to 1100°C over durations of $\sim$ 250 d to 55 yr (Figs. 12A, B). This result is consistent with both the Ryerson and McKeegan (1994) and Ingrin et al. (2001) diffusion calibrations for diopside. Likewise, diffusion during rapid cooling from high temperatures also provides a general fit to the oxygen isotopic patterns in these AOAs (Fig. 13). Cooling rates and timescales appear reasonable in the context of the duration of the solar nebula. Minimal exchange of FeO into olivine is consistent with a high-temperature setting for isotopic diffusion as olivine with significant Fa-content is not stable at high temperatures (e.g., Petaev and Wood, 1998). Based on these results, it is plausible that the Leoville AOAs underwent oxygen isotopic alteration in a high-temperature diffusion-dominated event.

4.2.3.3. Vigarano AOAs 65 and 66, CAI-67. The Vigarano AOAs and FGI show marked contrasts in oxygen isotopic and Fe-Mg compositional patterns. Vigarano AOA-65 is dominated by FeO-poor, ^{16}O-rich compositions suggesting minimal alteration after initial formation in a ^{16}O-rich, FeO-poor high-temperature setting. One of the six SIMS analyses from this AOA (B9-5; Table 2) has a partially ^{16}O-depleted composition, possibly reflecting rim compositions of fine-grained diopside and anorthite. All other analyses, including those dominated by anorthite (e.g., B10-2, Table 2) are ^{16}O-rich, indicating that any reheating events in the presence of a ^{16}O-poor gas or fluid must have been of short duration or at low temperature.

CAI-67 exhibits a similar isotopic pattern: dominated by ^{16}O-rich compositions but with one exceptional analysis (B10-04; Table 2) indicating partial oxygen isotopic exchange in melilite. This ^{16}O-depleted composition may be a consequence

of the effect of major element composition on diffusion rate in melilite (Yurimoto et al., 1989), or the OH-rich composition of this melilite (Fig. 9), or the fact that this analysis was collected along a crack (Fig. 7D) where migration of ^{16}O-poor fluid may have been localized. However, the most significant result from CAI-67 is that the diopside and two of three melilite analyses are ^{16}O-rich. The melilite analyses are particularly important because oxygen diffuses much more rapidly in melilite than in the common AOA phases (Yurimoto et al., 1989; Ryerson and McKeegan, 1994). Therefore, the results from this CAI conform to the results from AOA-65, indicating an origin in a ^{16}O-rich FeO-poor setting, followed by minor localized alteration.

In contrast to these two objects, AOA-66 shows evidence of substantial re-equilibration in a FeO-rich, ^{16}O-poor setting. Olivine from this AOA is distinctly zoned with rims of $\sim Fo_{70}$ and cores of $Fo_{\sim 96}$ (Table 1; Fig. 7C). The core compositions are particularly significant because they have incorporated more FeO than the forsterite cores in adjacent AOA-65. If this FeO-enrichment is a result of diffusion, then the Fe-Mg-zoning indicates fractional equilibration in excess of 0.6 ($f_{FeMg} \geq 0.6$; Fig. 10). At the same time, olivine cores and rims have remained ^{16}O-rich, while some interstitial grains are ^{16}O-poor (Table 2; Fig. 8).

Diffusion may have controlled elemental and oxygen isotopic compositions in AOA-66 olivine. Because of differences in diffusion rates, originally ^{16}O-rich, Fe-poor olivine is expected to undergo Fe-Mg-exchange before O-exchange during diffusion from a ^{16}O-poor, FeO-rich reservoir (Figs. 12A and 13A). Grain margins and newly crystallized interstitial grains may reflect the composition of a ^{16}O-poor altering reservoir, accounting for the ^{16}O-poor composition of analysis B13-6 (Table 2; also see Imai and Yurimoto, 2003). The distinct Fe-Mg and oxygen isotopic characteristics of AOA-66 indicate that this object evolved independently of adjacent objects AOA-65 and CAI-67, confirming previous interpretations that Vigarano is a breccia composed of Allende-like and reduced CV-like components (McSween, 1977; Krot et al., 2000).

4.3. Comparison of AOSs with CAIs: Implications for High-Temperature Nebular Processing

4.3.1. AOAs and CAIs may have come from the same nebular setting

The ^{16}O-rich 1st-generation signal of the AOAs examined in this study is common to most CAIs (Clayton et al., 1973, 1977; Yurimoto et al., 1994, 1998; McKeegan et al., 1998; Guan et al., 2000; Krot et al., 2001b; Fagan et al., 2001; Aléon et al., 2002). This similarity in oxygen isotopic composition combined with previous studies (Grossman and Steele, 1976; Komatsu et al., 2001, 2002; Chizmadia et al., 2002) suggest that AOAs may have formed by condensation in the same nebular region as CAIs, but at lower temperatures, followed by annealing and low-degree partial melting. In fact, there may be no functional difference in the 1st-generation origin of spinel-pyroxene-anorthite-rich CAIs and AOAs, except that they formed initially over slightly different temperature intervals.

The CAI-like domains enclosed within the reduced CV AOAs are dominated by Al-diopside, anorthite and spinel (this study; Komatsu et al., 2001), all having condensation temperatures similar to those of forsterite and FeNi-metal (Grossman, 1972; Petaev and Wood, 1998; Ebel and Grossman, 2000). The more refractory CAI minerals, such as corundum, hibonite, grossite, and melilite, are conspicuously absent. Of these minerals, only melilite has been reported from AOAs in general, and its occurrence is rare (Hashimoto and Grossman, 1987; Fagan et al., 2003). The paucity of highly refractory CAI-minerals in AOAs is consistent with efficient temperature-based sorting during 1st-generation processing.

4.3.2. AOAs and CAIs were altered under a variety of conditions

Even if discussion is limited to the AOAs and CAI examined in this study, multiple patterns in oxygen isotopic systematics are found. In the Efremovka AOAs, the FeO-rich, ^{16}O-depleted compositions of olivine rims combined with the more rapid diffusion rates of Fe-Mg than O imply that either: (1) O and Fe-Mg were decoupled during alteration of original olivine grains by diffusion, or (2) O and Fe-Mg alteration of AOAs occurred simultaneously by a mechanism other than diffusion, possibly dissolution and recrystallization. The OH-rich, ^{16}O-depleted analyses in Efremovka provide independent evidence that alteration of the Efremovka AOAs occurred in the presence of a hydrous fluid. In contrast, the distribution of oxygen isotopes among minerals in the Leoville AOAs can be explained as a consequence of diffusion during relatively short-term, high-temperature heating in the presence of a ^{16}O-poor gas in a nebular setting. Two contrasting patterns were identified in Vigarano. One AOA and CAI-67 exhibit minimal evidence of alteration after formation in a ^{16}O-rich, FeO-poor setting. The other AOA has undergone extensive FeO-alkali metasomatic alteration. The olivine in this AOA is zoned in Fe-Mg but has retained its ^{16}O-rich oxygen isotopic composition, and a mixed analysis of overlapping grain margins yields a ^{16}O-poor composition. This pattern is plausible for alteration and diffusive reequilibration in the presence of a ^{16}O-poor, FeO-rich fluid. The contrast between this AOA and the adjacent minimally-altered AOA and CAI indicate that the FeO-rich AOA was altered before assembly of the Vigarano parent body, possibly on a previous generation asteroid.

The isotopic patterns observed in the reduced CVs are diverse, yet they can all be explained as a consequence of diffusion and solid-gas or solid-aqueous fluid reactions that are plausible given estimates of the duration of the solar nebula and parent body metamorphism. This is not the case for coarse-grained type B CAIs, which require some mechanism to enhance the O-diffusion rate in melilite (Yurimoto et al., 1989; Ryerson and McKeegan, 1994) to account for the oxygen isotopic systematics of Type B CAIs (Clayton et al., 1977; Clayton, 1993; Yurimoto et al., 1994; Kim et al., 2002). It has been suggested that melilite in the Type B CAIs is melted during rapid heating and exchanges oxygen while molten with a surrounding ^{16}O-poor gas (Yurimoto et al., 1998). This model depends on kinetically favored melting of melilite under disequilibrium conditions (Greenwood and Hess, 1996). No similar type of event is required to account for the oxygen isotopic systematics in the AOAs of this study. However, a nebular

setting for isotopic exchange is plausible for Leoville AOAs-30 and -75.

These observations can be explained if refractory objects formed or were altered in a nebular setting that was subject to rapid variations in oxygen isotopic composition. This inference is consistent with the presence of ^{16}O-rich minerals in Wark-Lovering rims that surround CAIs having ^{16}O-poor melilite (Krot et al., 2002a; Yoshitake et al., 2002), and with oxygen isotopic variations of melilite from a single CAI (Harazono and Yurimoto, 2003). The general correlation between igneous textures and ^{16}O-depletions in CAIs from CR-chondrites also supports a model where refractory objects experienced reheating in a nebular setting with varying oxygen isotopic compositions (Aléon et al., 2002). Variations in isotopic composition linked to thermal fluctuations can be accounted for by the X-wind model (Shu et al., 1996) as a consequence of radial oscillations in location of the X-point and consequent oscillations in dust:gas ratios in the region where AOAs and CAIs formed (Yurimoto et al., 2001; Itoh and Yurimoto, 2003). Changes in isotopic composition also may have resulted from variations in the extent of mass-independent fractionation (Thiemens and Heidenreich, 1983; Thiemens, 1999), or from turbulent drift of refractory solids into isotopically distinct regions of the nebula (Cuzzi et al., 2003).

5. CONCLUSIONS

A common setting for the origin of AOAs and CAIs is credible based on mineral assemblages, textures, elemental compositions and oxygen isotopic ratios. Thus it is possible that AOAs and CAIs formed in the same regions and from the same parcels of gas, but were sorted by condensation over distinct temperature ranges. Temperature-based sorting has also been called upon to explain the distribution of CAIs among members of the CR-clan (Weber and Bischoff, 1994, 1997; Krot et al., 2002b). Of course, zoning patterns, Wark-Lovering rims, and isotopic distributions indicate that some CAIs underwent complex thermal histories, but many refractory objects, including most AOAs, probably formed initially over limited temperature ranges before separation from reactive gas.

The AOAs examined here show variable depletions in ^{16}O, reflecting alteration under different conditions. Correlated ^{16}O-depletion and FeO-enrichment in olivine rims in two AOAs from Efremovka probably originated by dissolution and precipitation in the presence of an aqueous fluid in a parent body setting (Kojima et al., 1993; Kojima and Tomeoka, 1996; Krot et al., 1995, 1998). This hypothesis is consistent with elevated OH detected during SIMS analyses of ^{16}O-depleted domains. Elevated OH also correlates with ^{16}O-depletion in a melilite-pyroxene CAI from Vigarano, suggesting isotopic exchange in an aqueous environment. This CAI occurs adjacent to two AOAs: one is unaltered, but the other has undergone FeO-alkali metasomatism and alteration in a ^{16}O-poor setting. The contrast between these adjacent objects indicates that the FeO-alkali metasomatic event preceded accretion of the Vigarano parent body, and may have occurred on a previous asteroid.

In contrast, two AOAs from Leoville have oxygen isotopic patterns that can be attributed to diffusional exchange during a high-temperature event. The Leoville AOAs have ^{16}O-rich olivine, Al-diopside with variable intermediate compositions and ^{16}O-poor anorthite. These results can be modeled for AOA grain sizes as a result of exchange with a ^{16}O-poor reservoir during heating to ~ 900 to 1100°C over durations of ~ 250 d to 55 yr, consistent with a dynamic nebular setting with spatial or temporal transitions in temperature and oxygen isotopic composition occurring on timescales of months to years.

Acknowledgments—This work was supported by a postdoctoral fellowship from the Japan Society for the Promotion of Science (T. J. Fagan), NASA Grants NAG 5-4212 and NAG 5-11591 (K. Keil, P. I.), NASA Grant NAG5-13131 (A. N. Krot, P. I.), and a Monbu-kagaku-sho grant. Polished thin sections of Efremovka and Vigarano were provided by J. Goswami of the Physical Research Lab, Ahmedabad, India, and Tim McCoy and Linda Welzenbach of the Smithsonian Institution, Washington, DC, USA. We thank M. Itoh, M. Yoshitake and K. Nagashima for assistance with SIMS analyses, and the E. Takahashi lab group for assistance with EPMA analyses. The senior author spent 2 years on a fellowship in Japan and is grateful for the warm hospitality extended to him by the faculty, postdocs, students and administrative staff at Tokyo Institute of Technology. The manuscript was improved by careful reviews by Paul Buchanan and Gary Huss. This is Hawaii Institute of Geophysics and Planetology publication No. 1315 and School of Ocean and Earth Science and Technology publication No. 6312.

Associate editor: C. Koeberl

REFERENCES

Aléon J., Krot A. N., and McKeegan K. D. (2002) Calcium-aluminum-rich inclusions and amoeboid olivine aggregates from the CR carbonaceous chondrites. *Meteorit. Planet. Sci.* **37,** 1729–1755.

Ando K. and Oishi Y. (1983) Effect of ratio of surface area to volume on oxygen self-diffusion coefficients determined for crushed MgO-Al_2O_3 spinels. *J. Am. Ceram. Soc.* **66,** C131–C132.

Buening D. K. and Buseck P. R. (1973) Fe-Mg lattice diffusion in olivine. *J. Geophys. Res.* **78,** 6852–6862.

Chakraborty S. (1997) Rates and mechanisms of Mg-Fe interdiffusion in olivine at 980 C–1300 C. *J. Geophys. Res.* **102,** 12317–12331.

Chakraborty S., Farver J. R., Yund R. A., and Rubie D. C. (1994) Mg tracer diffusion in synthetic forsterite and San Carlos olivine as a function of P, T, and fO_2. *Phys. Chem. Mineral* **21,** 489–500.

Chizmadia L. J., Rubin A. E., and Wasson J. T. (2002) Mineralogy and petrology of amoeboid olivine inclusions in CO3 chondrites: Relationship to parent-body aqueous alteration. *Meteorit. Planet. Sci.* **37,** 1781–1796.

Clayton R. N. (1993) Oxygen isotopes in meteorites. *Ann. Rev. Earth Planet. Sci.* **21,** 115–149.

Clayton R. N. and Mayeda T. K. (1999) Oxygen isotope studies of carbonaceous chondrites. *Geochim. Cosmochim. Acta.* **63,** 2089–2104.

Clayton R. N., Grossman L., and Mayeda T. K. (1973) A component of primitive nuclear composition in carbonaceous meteorites. *Science* **182,** 485–488.

Clayton R. N., Onuma N., Grossman L., and Mayeda T. K. (1977) Distribution of the pre-solar component in Allende and other carbonaceous chondrites. *Earth Planet. Sci. Lett.* **34,** 209–224.

Crank J. (1975) *The Mathematics of Diffusion*. Clarendon Press.

Cuzzi J. N., Davis S. S., and Dobrovolskis A. R. (2003) Creation and distribution of CAIs in the protoplanetary nebula. *Lunar Planet. Sci.* **34,** 1749.

Ebel D. S. and Grossman L. (2000) Condensation in dust-enriched systems. *Geochim. Cosmochim. Acta.* **64,** 339–366.

Elphick S. C., Graham C. M., and Denis P. F. (1988) An ion microprobe study of anhydrous diffusion in anorthite: A comparison with hydrothermal data and some geological implications. *Contr. Mineral. Petrol* **100,** 490–495.

Fagan T. J., Krot A. N., and Keil K. (2000) Calcium-aluminum-rich inclusions in enstatite chondrites (I): Mineralogy and textures. *Meteorit. Planet. Sci.* **35,** 771–781.

Fagan T. J., McKeegan K. D., Krot A. N., and Keil K. (2001) Calcium-aluminum-rich inclusions in enstatite chondrites (II): Oxygen isotopes. *Meteorit. Planet. Sci.* **36,** 223–230.

Fagan T. J., Yurimoto H., Krot A. N., and Keil K. (2002) Similarities and differences in oxygen isotopic evolution of fine vs coarse refractory inclusions in the reduced CV3 Efremovka. *Meteorit. Planet. Sci.* **37,** A45.

Fagan T. J., Krot A. N., and Yurimoto H. (2003) Petrology and oxygen isotope compositions of refractory inclusions from Acfer 094. *Lunar Planet. Sci.* **34,** 1274.

Gérard O. and Jaoul O. (1989) Oxygen diffusion in San Carlos olivine. *J. Geophys. Res.* **94,** 4119–4128.

Greenwood J. P. and Hess P. C. (1996) Congruent melting kinetics: Constraints on chondrule formation. In *Chondrules and the Protoplanetary Disk* (eds. R. H. Hewins, R. H. Jones, and E. R. D. Scott), pp. 205–211. Cambridge University Press.

Grossman L. (1972) Condensation in the primitive solar nebula. *Geochim. Cosmochim. Acta.* **36,** 597–619.

Grossman L. (1975) Petrography and mineral chemistry of Ca-rich inclusions in the Allende meteorite. *Geochim. Cosmochim. Acta.* **39,** 433–454.

Grossman L. and Steele I. M. (1976) Amoeboid olivine aggregates in the Allende meteorite. *Geochim. Cosmochim. Acta.* **40,** 149–155.

Grossman L. Fedkin A. V. (2003) Elemental abundance constraints on condensation of Allende matrix olivine. In *Evolution of Solar System Materials: A New Perspective from Antarctic Meteorites,* pp. 31–32. National Institute of Polar Research, International Symposium.

Guan Y., McKeegan K. D., and MacPherson G. J. (2000) Oxygen isotopes in calcium-aluminum-rich inclusions from enstatite chondrites: New evidence for a single CAI source in the solar nebula. *Earth Planet. Sci. Lett.* **181,** 271–277.

Guimon R. K., Symes S. J. K., Sears D. W. G., and Benoit P. H. (1995) Chemical and physical studies of type 3 chondrites XII: The metamorphic history of CV chondrites and their components. *Meteoritics* **30,** 704–714.

Harazono K. and Yurimoto H. (2003) Oxygen isotopic variations in a fluffy Type A CAI from the Vigarano meteorite. *Lunar Planet. Sci.* **34,** 1540.

Hashimoto A. and Grossman L. (1987) Alteration of Al-rich inclusions inside amoeboid olivine aggregates in the Allende meteorite. *Geochim. Cosmochim. Acta.* **51,** 1685–1704.

Hiyagon H. and Hashimoto A. (1999) ^{16}O excesses in olivine inclusions in Yamato-86009 and Murchison chondrites and their relation to CAIs. *Science* **283,** 828–831.

Imai H. and Yurimoto Y. H. (2003) Oxygen isotopic distribution in an amoeboid olivine aggregate from the Allende CV chondrite: Primary and secondary processes. *Geochim. Cosmochim. Acta.* **67,** 765–772.

Ingrin J., Pacaud L., and Olivier J. (2001) Anisotropy of oxygen diffusion in diopside. *Earth Planet. Sci. Lett.* **192,** 347–361.

Itoh S., Rubin A. E., Kojima H., Wasson J. T., and Yurimoto H. (2002) Amoeboid olivine aggregates and an AOA-bearing chondrule from Y-81020 CO 3.0 chondrite: Distribution of oxygen and magnesium isotopes. *Lunar Planet. Sci.* **33,** 1490.

Itoh S. and Yurimoto H. (2003) Contemporaneous formation of chondrules and refractory inclusions in the early Solar System. *Nature* **423,** 728–731.

Jaoul O., Froidevaux C., Durham W. B., and Michaut M. (1980) Oxygen self-diffusion in forsterite: Implications for the high temperature creep mechanism. *Earth Planet. Sci. Lett.* **47,** 391–397.

Jaoul O., Houlier B., and Abel F. (1983) Study of ^{18}O diffusion in magnesium orthosilicate by nuclear microanalysis. *J. Geophys. Res.* **88,** 613–624.

Jones R. H., Lee T., Connolly H. C. Jr., Love S. G., and Shang H. (2000) Formation of chondrules and CAIs: Theory vs. observation. In *Protostars and Planets IV* (eds. V. Mannings, A. P. Bass and S. S. Russell), University of Arizona Press, Tucson, pp. 927–962.

Jurewicz A. J. G. and Watson E. B. (1988) Cations in olivine, Part 2: Diffusion in olivine xenocrysts, with applications to petrology and mineral physics. *Contr. Mineral. Petrol* **99,** 186–201.

Kaiser T. and Wasserburg G. J. (1983) The isotopic composition and concentration of Ag in iron meteorites and the origin of exotic silver. *Geochim. Cosmochim. Acta.* **47,** 43–58.

Kim G. L., Yurimoto H., and Sueno S. (2002) Oxygen isotopic composition of a compound Ca-Al-rich inclusion from Allende meteorite: Implications for origin of palisade bodies and O-isotopic environment in the CAI forming region. *J. Mineral. Petrol. Sci.* **97,** 161–167.

Kojima T., Tomeoka K., and Takeda H. (1993) Unusual dark clasts in the Vigarano CV3 carbonaceous chondrite: Record of parent body process. *Meteoritics* **28,** 649–658.

Kojima T. and Tomeoka K. (1996) Indicators of aqueous alteration and thermal metamorphism on the CV parent body: Microtextures of a dark inclusion from Allende. *Geochim. Cosmochim. Acta.* **60,** 2651–2666.

Komatsu M., Krot A. N., Petaev M. I., Ulyanov A. A., Keil K., and Miyamoto M. (2001) Mineralogy and petrography of amoeboid olivine aggregates from the reduced CV3 chondrites Efremovka, Leoville and Vigarano: Products of nebular condensation and accretion. *Meteorit. Planet. Sci.* **36,** 629–641.

Komatsu M., Miyamoto M., Mikouchi T., Krot A. N., and Keil K. (2002) Heating experiments of olivine-anorthite mixtures: Clues to understanding the textural relationships among olivine, Al-diopside and anorthite in amoeboid olivine aggregates. *Lunar Planet. Sci.* **33,** 1258.

Kornacki A. S. and Wood J. A. (1984) Petrography and classification of Ca,Al-rich and olivine-rich inclusions in the Allende CV3 chondrite. *Lunar. Planet. Sci.* **14,** B573–B587.

Krot A. N., Scott E. R. D., and Zolensky M. E. (1995) Mineralogical and chemical modification of components in CV3 chondrites: Nebular or asteroidal processing. *Meteoritics* **30,** 748–776.

Krot A. N., Petaev M. I., Scott E. R. D., Choi B.-G., Zolensky M. E., and Keil K. (1998) Progressive alteration in CV3 chondrites: More evidence for asteroidal alteration. *Meteorit. Planet. Sci.* **33,** 1065–1085.

Krot A. N., Meibom A., and Keil K. (2000) A clast of Bali-like oxidized CV material in the reduced CV chondrite breccia Vigarano. *Meteorit. Planet. Sci.* **35,** 817–825.

Krot A. N., McKeegan K. D., Russell S. S., Meibom A., Weisberg M. K., Zipfel J., Krot T. V., Fagan T. J., and Keil K. (2001a) Refractory calcium-aluminum-rich inclusions and aluminum-diopside-rich chondrules in the metal-rich chondrites Hammadah al Hamra 237 and QUE 94411. *Meteorit. Planet. Sci.* **36,** 1189–1217.

Krot A. N., Ulyanov A. A., Meibom A., and Keil K. (2001b) Forsterite-rich accretionary rims around Ca,Al-rich inclusions from the reduced CV3 chondrite Efremovka. *Meteorit. Planet. Sci.* **36,** 611–628.

Krot A. N., McKeegan K. D., Leshin L. A., MacPherson G. J., and Scott E. R. D. (2002a) Existence of an ^{16}O-rich gaseous reservoir in the solar nebula. *Science* **295,** 1051–1054.

Krot A. N., Meibom A., Weisberg M. K., and Keil K. (2002b) The CR chondrite clan. Implications for early solar system processes. *Meteorit. Planet. Sci.* **37,** 1451–1490.

Lee M. R., Hutchison R., and Graham A. L. (1996) Aqueous alteration in the matrix of the Vigarano (CV3) carbonaceous chondrite. *Meteorit. Planet. Sci.* **31,** 477–483.

MacPherson G. J., Wark D. A., and Armstrong J. T. (1988) Primitive material surviving in chondrites: Refractory inclusions. In *Meteorites and the Early Solar System* (eds. J. F. Kerridge and M. S. Matthews), pp. 746–807. University of Arizona Press.

MacPherson G. J. and Krot A. N. (2002) Distribution of Ca-Fe-silicates in CV3 chondrites. Possible controls by parent-body compaction. *Meteorit. Planet. Sci.* **37,** A91.

Makide K., Fukusawa Y., Yurimoto H., and Nagawa H. (2002) Remelting/recrystallization experiment on a Ca, Al-rich system using Sr and Ba as tracers. *Meteorit. Planet. Sci.* **37,** A92.

McKeegan K. D., Leshin L. A., Russell S. S., and MacPherson G. J. (1998) Oxygen isotopic abundances in calcium-aluminum-rich inclusions from ordinary chondrites: Implications for nebular heterogeneity. *Science* **280,** 414–418.

McSween H. Y., Jr.. (1977) Petrographic variations among carbonaceous chondrites of the Vigarano type. *Geochim. Cosmochim. Acta.* **41,** 1777–1790.

Michel-Lévy M. C. (1986) Étude comparative des chondrites carbonées d'Allende et de Léoville I. Minéralogie, pétrographie, chimie. *Bull. Mus. Nat. Hist. Natural. Ser. 4* **8,** 89–147 section C.

Misener D. J. (1974) Cationic diffusion in olivine to 1400°C and 35 kbar. In *Geochemical Transport and Kinetics* (eds. A. W. Hofmann, G. J. Giletti, H. S. Yoder, Jr, and R. A. Yund), pp. 117–129. Carnegie Institute of Washington.

Miyamoto M., Mikouchi T., and Arai T. (2002) Comparison of Fe-Mg interdiffusion coefficients in olivine. *Antarct. Meteorite Res.* **15,** 143–151.

Nakamura A. and Schmalzried H. (1983) On the nonstoichiometry and point defects of olivine. *Phys. Chem. Mineral* **10,** 27–37.

Petaev M. I. and Wood J. A. (1998) The condensation with partial isolation (CWPI) model of condensation in the solar nebula. *Meteorit. Planet. Sci.* **33,** 1123–1137.

Reddy K. P. R., Oh S. M., Major L. D., and Cooper A. R. (1980) Oxygen diffusion in forsterite. *J. Geophys. Res.* **85,** 322–326.

Reddy K. P. R. and Cooper A. R. (1981) Oxygen diffusion in magnesium aluminate spinel. *J. Am. Ceram. Soc.* **64,** 368–371.

Russell S. S., Huss G. R., Fahey A. J., Greenwood R. C., Hutchison R., and Wasserburg G. J. (1998) An isotopic and petrologic study of calcium-aluminum-rich inclusions from CO3 meteorites. *Geochim. Cosmochim. Acta.* **62,** 689–714.

Ryerson F. J., Durham W. B., Cherniak D. J., and Lanford W. A. (1989) Oxygen diffusion in olivine: Effect of oxygen fugacity and implications for creep. *J. Geophys. Res.* **94,** 4105–4118.

Ryerson F. J. and McKeegan K. D. (1994) Determination of oxygen self-diffusion in åkermanite, anorthite, diopside, and spinel: Implications for oxygen isotopic anomalies and the thermal histories of Ca-Al-rich inclusions. *Geochim. Cosmochim. Acta.* **58,** 3713–3734.

Sahijpal S., McKeegan K. D., Krot A. N., Weber D., and Ulyanov A. A. (1999) Oxygen-isotopic compositions of calcium-aluminum-rich inclusions from the CH chondrites, Acfer 182 and Patuxtent Range 91546. *Meteorit. Planet. Sci.* **34,** A101.

Scott E. R. D., Keil K., and Stöffler D. (1992) Shock metamorphism of carbonaceous chondrites. *Geochim. Cosmochim. Acta.* **56,** 4281–4293.

Shu F. H., Shang H., and Lee T. (1996) Toward an astrophysical theory of chondrites. *Science* **271,** 1545–1552.

Thiemens M. H. (1999) Mass-independent isotope effects in planetary atmospheres and the early solar system. *Science* **283,** 341–345.

Thiemens M. H. and Heidenreich J. E., III. (1983) The mass-independent fractionation of oxygen: A novel isotope effect and its possible cosmochemical implications. *Science* **219,** 1073–1075.

Wasson J. T., Yurimoto H., and Russell S. S. (2001) ^{16}O-rich melilite in the CO3.0 chondrites. Possible formation of common, ^{16}O-poor melilite by aqueous alteration. *Geochim. Cosmochim. Acta.* **65,** 4539–4549.

Weber D. and Bischoff A. (1994) The occurrence of grossite ($CaAl_4O_7$) in chondrites. *Geochim. Cosmochim. Acta.* **58,** 3855–3877.

Weber D. and Bischoff A. (1997) Refractory inclusions in the CR chondrite Acfer 059-El Djouf 001: Petrology, chemical composition, and relationship to inclusion populations in other types of carbonaceous chondrites. *Chem. Erde.* **57,** 1–24.

Weinbruch S., Armstrong J., and Palme H. (1994) Constraints on the thermal history of the Allende parent body as derived from olivine-spinel thermometry and Fe/Mg interdiffusion in olivine. *Geochim. Cosmochim. Acta.* **58,** 1019–1030.

Wilson L., Keil K., Browning L. B., Krot A. N., and Bourcier W. (1999) Early aqueous alteration, explosive disruption, and re-processing of asteroids. *Meteorit. Planet. Sci.* **34,** 541–557.

Yoshitake M., Yoshiyuki K., and Yurimoto H. (2002) Distributions of O isotopes in Wark-Lovering rim of a Type B2 CAI from the Vigarano meteorite. *Lunar Planet. Sci.* **33,** 1502.

Young E. D. and Russell S. S. (1998) Oxygen reservoirs in the early solar nebula inferred from an Allende CAI. *Science* **282,** 452–455.

Yurimoto H., Morioka M., and Nagasawa H. (1989) Diffusion in single crystals of melilite: I. Oxygen. *Geochim. Cosmochim. Acta.* **53,** 2387–2394.

Yurimoto H., Nagasawa H., Mori Y., and Matsubaya O. (1994) Micro-distribution of oxygen isotopes in a refractory inclusion from the Allende meteorite. *Earth Planet. Sci. Lett.* **128,** 47–53.

Yurimoto H., Ito M., and Nagasawa H. (1998) Oxygen isotope exchange between refractory inclusion in Allende and solar nebula gas. *Science* **282,** 1874–1877.

Yurimoto H., Asada Y., and Hirai K. (2001) Oxygen isotopic composition of fine-grained CAIs and genetic relation to coarse-grained CAIs. *Meteorit. Planet. Sci.* **36,** A230.